Beyond deep versus superficial: true laminar inference with MEG

Maciej J. Szul[1,2,3], Ishita Agarwal[1,2,4], Quentin Moreau[1,2], Bassem Hiba[1,2], Sven Bestmann[5,6], Gareth R. Barnes[5], James J. Bonaiuto[1,2]

[1]Institut des Sciences Cognitives Marc Jeannerod, CNRS UMR 5229, Lyon, France, [2]Université Claude Bernard Lyon 1, Université de Lyon, France, [3]Department of Psychiatry and Psychotherapy, Faculty of Medicine, University of Tübingen, [4]Department of Psychological Sciences, Purdue University, West Lafayette, Indiana, USA, [5]Department of Imaging Neuroscience, UCL Queen Square Institute of Neurology, University College London, London, UK, [6]Department of Clinical and Movement Neurosciences, UCL Queen Square Institute of Neurology, University College London, London, UK

Correspondence: James J Bonaiuto (james.bonaiuto@isc.cnrs.fr)

Keywords: high-precision MEG (hpMEG), laminar inference, source localization, cortical laminae, cortical columnar organization

Abstract

Neural dynamics at the laminar level are critical components of cortical computations, but in humans, non-invasive methods to study these dynamics have been limited to coarse distinctions between deep and superficial layers. Here, we demonstrate that high-precision magnetoencephalography (hpMEG) can achieve laminar inference by localizing sources across all six cortical laminae. Using a multilayer source reconstruction approach, we systematically assess the limits of hpMEG's depth resolution, and show that laminar precision is achievable under optimal signal-to-noise ratios and co-registration accuracy. Our simulations reveal that accurate source reconstruction depends critically on aligning dipole orientations with the underlying cortical columnar structure, and that regional variations in cortical anatomy influence reconstruction fidelity. These findings position hpMEG as a powerful tool for investigating laminar-specific neural dynamics in cognition and behavior, and offer new opportunities to bridge invasive electrophysiology and human neuroimaging.

Introduction

The morphology, connectivity, and computations of cortical laminae have been central topics in neuroscience for over a century (*1*). Laminar electrophysiology has provided otherwise inaccessible insights into fundamental sensory and sensorimotor computations, such as laminar specific receptive fields (*2*) and the directional flow of information in feed-forward and feedback pathways (*3–6*). In cognitive neuroscience, the integration of predictive coding with laminar interaction models (canonical microcircuits) has led to mechanistic hypotheses about the role of laminar-specific activity in cognition (*4*, *7–20*). Clinically, assessment of laminar dynamics has improved our understanding of epileptogenic propagation (*21*, *22*) and holds promise for refining our knowledge of disorders such as Parkinson's disease (*23*), but these investigations have been mostly limited to invasive methods.

Invasive electrophysiological recordings are widely used in animal models, whereas they are typically restricted to clinical populations in humans. (*24–26*). Traditional invasive recordings provide direct access to neuronal events, capturing single-unit and local population activity with high spatial and temporal resolution, though newer technologies such as Neuropixels now extend this access across entire cortical columns and brain structures (*27*, *28*). However, their use requires surgical implantation, necessitating ethical considerations in animal research, and medical justification in human studies. Although invasive recordings enable laminar-level recordings in cortex, they remain extracellular and thus are still subject to an inverse problem (*29*). This limitation has motivated recent efforts to develop magnetrodes, which aim to directly measure intracellular currents (*30*). Nevertheless, these invasive methods are not feasible for broader applications in cognitive neuroscience. In contrast, non-invasive methods like electroencephalography (EEG), magnetoencephalography (MEG), and functional magnetic resonance imaging (fMRI) dominate human neuroscience due to their practicality and ethical viability (*31–33*). Their whole brain coverage enables the study of network-level processing, but each modality has inherent limitations. EEG and MEG provide high temporal resolution, but are thought to lack the spatial specificity needed for laminar inference (*33–40*), whereas fMRI has excellent spatial, but poor temporal resolution (*31*, *41–43*). Recent advances in high resolution fMRI have enabled laminar-level analysis, but its inherently limited temporal resolution precludes the study of laminar dynamics (*44–47*).

MEG has traditionally been considered incapable of resolving sources with a precision at or below the thickness of the cortex (*39*, *48–51*). However, this assumption has been challenged by studies indicating that there is no fundamental theoretical barrier to achieving high spatial resolution with MEG; the primary limitation is the practical issue of signal-to-noise ratio (SNR). With sufficiently high SNR, facilitated by techniques such as precise head-casts to minimize co-registration errors, MEG could, in principle, resolve sources with much finer precision than traditionally assumed (*52*, *53*). Achieving high signal quality in actual recordings requires minimizing co-registration errors, between-session head position variability, and within-session movement, all of which has been addressed using customized head-casts that stabilize the head relative to the sensor array (*54–56*). hpMEG spurred the development of early laminar MEG approaches, which involved Bayesian model comparison between separate forward models for two cortical depths: deep and superficial, or analysis of source signals using a forward model combining surfaces for the two layers (*52*, *53*, *57*). These approaches have been used to successfully detect laminar differences

predicted by theoretical models and invasive recordings, such as laminar-specific spectral activity (*57*) and distinct laminar signatures of beta bursts (*58*). However, previous studies have been limited to bilaminar distinctions (deep vs. superficial).

Here, we demonstrate that hpMEG can resolve sources across all six cortical laminae. We expand the source space to include an arbitrary number of intermediate layers. We refer to the equidistant depth surfaces used in our forward models as layers (denoted with Arabic numerals, i.e. 1-11), while we use laminae (denoted with Roman numerals) to refer to cytoarchitectonically defined cortical layers (i.e. I-VI), and systematically probe the limits of data quality required for true laminar precision. We show that accurate laminar inference critically depends on aligning the dipole orientations in the forward model with the true cortical column orientations. Finally, we demonstrate that variations in anatomical features across the cortex leads to regionally varying reconstruction precision, consistent with prior findings (*53*). This positions hpMEG as a powerful tool for interrogating neural circuits at a laminar level, offering new opportunities to study how computations within and across cortical layers shape network-level interactions underlying cognition and behavior.

Methods

Data Acquisition

MRI data were collected from a single volunteer using a 3T MRI scanner in two separate protocols. The first protocol generated a precise scalp image for head-cast construction (*55*). It used a T1-weighted 3D FLASH sequence with 1 mm isotropic resolution and a field of view of 256 × 256 × 192 mm (A–P, H–F, R–L). The repetition time was 7.96 ms, with a 12° flip angle, and a single echo was acquired per excitation. A high readout bandwidth (425 Hz/pixel) minimized geometric distortions, and the 3 min 42 s scan duration reduced motion sensitivity. To avoid distortions from skin displacement, a spacious 12-channel head coil was used without padding or headphones. The participant-specific MEG head-cast was created to minimize head movement during MEG recordings using a 3D scalp model extracted from T1-weighted images using SPM (*54*, *55*). A Zcorp 3D printer produced the model, which was then placed in a dewar replica and filled with polyurethane foam to form the head-cast. The head-cast model included fiducial coil protrusions which became indentations in the foam, ensuring accurate coil placement during MEG scanning (*55*).

The second protocol used a quantitative multi-parameter mapping (MPM) approach, consisting of three 3D FLASH acquisitions, with proton density (PD), T1, and magnetization transfer (MT) weighting, alongside calibration sequences to correct RF transmit field inhomogeneities. Data were acquired at 800 µm isotropic resolution, using specific flip angles (6° for PD/MT, 21° for T1), and applying Gaussian RF pulses for MT weighting. Gradient echoes were sampled at multiple echo times, with parallel imaging (GRAPPA, factor of 2) accelerating acquisition. Transmit field inhomogeneities and geometric distortions were corrected following established methods, and quantitative maps (PD, R1, MT, and R2*) were computed. The entire acquisition lasted less than 30 minutes (*53*, for details see *57*). A custom FreeSurfer-based (v6.0.1) reconstruction procedure was used to generate pial and white/grey matter boundary surfaces from the PD and T1 volumes of the MPMs (Figure 1a).

MEG data were recorded using a 275-channel CTF system with SQUID-based axial gradiometers in a magnetically shielded room. Data was digitized continuously at 1200 Hz.

The MEG sensor data of this subject were not used; the dataset served only to define the sensor layout, sampling rate (1200 Hz, downsampled to 600 Hz), trial count (531), and sample count (1201) for simulations.

Preprocessing

We used FreeSurfer's *mris_expand* function (v6.0.1; *59*) to generate 9 equidistant intermediate surfaces between the pial boundary surface and white matter boundary surface, yielding 11 cortical surfaces in total (Figure 1b). An arbitrary number of surfaces could be used, but we chose 11 for computational efficiency. These intermediate surfaces are not meant to represent the 6 cortical laminae, but rather to sample the cortical depth like a laminar electrode with multiple, evenly spaced contacts. Freesurfer operates on hemispheres independently, resulting in deep vertices and mesh faces cutting through subcortical structures. These vertices and associated faces were removed from each hemisphere of each layer mesh. The left and right hemisphere meshes of each intermediate surface were then combined by concatenation of their vertices and faces (left then right).

The resulting bihemispheric meshes each contained approximately 300,000 vertices, exceeding computational feasibility for source reconstruction. FreeSurfer generates the pial mesh by expanding the white matter boundary mesh until the pial boundary is reached. This results in a perfect correspondence between the vertices of each mesh: every pial mesh vertex has a matching white matter mesh vertex. The vectors linking these corresponding vertices, known as link vectors (*60*), have been shown to provide the best estimate of cortical column orientation out of available methods (*61*). One advantage of link vectors for constraining dipole orientation is that the vectors are equivalent across corresponding vertices in all intermediate surfaces. This ensures that model-based laminar comparison is based solely on dipole location. However, most methods for mesh downsampling disrupt the correspondence between vertices when applied independently to each layer as they alter vertex coordinates rather than simply removing vertices. We therefore downsampled the pial boundary surface by a factor of 10, using the *vtkDecimatePro* function of the VTK library (v9.3.0; *62*) because it is purely subtractive (i.e. it only removes vertices). We then downsampled the other 10 meshes by removing the same vertices that were removed from the pial surface, thus preserving vertex correspondence, and copying the pial mesh face structure (i.e. edges between vertices *61*). This enabled a straightforward computation of link vectors (Figure 1c), which were used to constrain dipole orientations in all of the main simulations and analyses.

Simulations

We tested the efficacy of each analysis method using synthetic datasets based on a real experimental recording of the same human participant whose MRI scans were acquired. The dataset was used to define the sensor layout, sampling rate (600 Hz), number of trials (531), and number of samples (1201) for the simulations; the MEG sensor data itself was discarded. All simulations and analyses were implemented using the laMEG software package (https://github.com/danclab/laMEG), built on a custom version of SPM (*63*) compiled as a python library (https://github.com/danclab/spm), and are available at http://github.com/danclab/multilaminar_sim.

For each simulation, we specified a source centered at a vertex on one of the 11 cortical surfaces spanning the depth of the cortex from the pial to the white matter surface. We simulated a localized patch of current density with a Gaussian-shaped temporal profile over a 2 s time window with a peak at the center of the window and full width at half maximum (FWHM) of 400 ms (time course displayed in Figure S1). The spatial extent of the simulated source was set to 5 mm FWHM (corresponding to a mean patch size of 14.93 vertices). To generate synthetic MEG data, we used a single-shell forward model (*64*) based on a surface composed of the 11 cortical layer meshes concatenated into a single mesh. The dipole moment for each simulation was set to 10 nAm unless otherwise specified. We selected 100 random cortical locations (vertices on the pial surface) and conducted separate simulations for different sensor-level signal-to-noise ratio (SNR) levels (-500, -50, -35, -20, -10, -5, 0, and 5 dB) and co-registration error levels (0, 0.5, 1, 2, 3, 4, and 5 mm). White noise was added at the sensor level, scaled to achieve the desired per-trial SNR (computed as the ratio of signal power to noise power across all sensors; , *53*). To introduce co-registration error, we perturbed the fiducial points used for MEG-MRI alignment by applying a combination of random translation and rotation to the nasion (NAS), left preauricular (LPA), and right preauricular (RPA) points. Fiducial coordinates were extracted from the subject's MRI and centered by subtracting their mean, a random translation vector was then generated, scaled to the specified error level (in mm), and applied to the fiducials, and a random rotation was applied, with a rotation angle drawn from a normal distribution scaled to match the specified error level (in degrees). The transformed fiducial locations were then used for MEG-MRI coregistration, simulating misalignment between the subject's head position in the MEG scanner and their anatomical MRI (*53*).

To evaluate the accuracy of laminar source reconstruction in the presence of multiple simultaneous sources, we conducted a separate set of simulations in which two sources of equal strength were generated at different cortical depths. For each of the 100 selected cortical locations, we fixed one source in the middle layer while systematically varying the second source from the most superficial to the deepest cortical surface. The simulated sources followed the same Gaussian-shaped temporal profile as in the single-source simulations, with a dipole moment of 10 nAm and a spatial extent of 5 mm FWHM. Synthetic MEG data were generated using a single-shell forward model, with white noise added to achieve a sensor-level SNR of -20 dB.

To evaluate the impact of different cortical column orientation estimation methods on laminar source reconstruction accuracy, we systematically varied the approach used to define dipole orientations during both simulation and reconstruction. We tested seven distinct methods, including surface normal vectors computed from the original high-resolution mesh (*61*) and a downsampled surface mesh (*65–68*), cortical patch statistics (*69*), and link vectors (*60*), with additional conditions for whether dipole orientations were fixed across layers. For each method, we simulated sources at the 100 selected cortical locations, assigning simulated dipole orientations based on the selected approach and then reconstructing sources using each of the different orientation definitions. The downsampled surface normal method estimated dipole orientation at each vertex of the decimated cortical mesh by averaging the normal vectors of all adjacent triangular faces. This was implemented using the *spm_mesh_normals* function in SPM (*63*). The original surface normal method followed the same approach but was applied to the full-resolution cortical surface before being mapped onto the decimated mesh for source localization (*61*). The cortical patch statistics method

calculated the mean normal vector at each vertex of the downsampled mesh using all neighboring vertices from the original high-resolution surface (*69*). In contrast, the link vector method defined dipole orientation as the vector linking each pial surface vertex to its corresponding white matter vertex (*60*), leveraging the one-to-one correspondence maintained during mesh decimation. Because different orientation estimation methods can yield subtly different vector fields, we assessed the angular discrepancies between these definitions and their effects on laminar inference accuracy. Dipole orientation vectors derived from each method were incorporated into the lead field matrix used for source inversion (*61*) in order to evaluate how orientation differences impact model evidence and depth localization accuracy across simulations. For each of these methods, we tested versions where the orientation was computed independently for each layer and versions where it was computed on the pial surface and fixed across layers (except for the link vectors method which is equivalent across layers by definition).

To examine how anatomical features influence the accuracy of laminar source reconstruction, we generated a large-scale set of simulations in which sources were placed at every vertex of a layered cortical mesh (one source per simulation). The mesh consisted of 29,130 locations at 11 cortical depths, resulting in a total of 320,420 simulated sources. Each simulation used a Gaussian-shaped temporal profile with a full width at half maximum (FWHM) of 400 ms and a dipole moment of 10 nAm (Figure S1 includes the time course of this simulated signal). Synthetic MEG data were generated using a single-shell forward model, and white noise was added to yield a sensor-level SNR of -20 dB. All of these simulations were conducted with zero co-registration error.

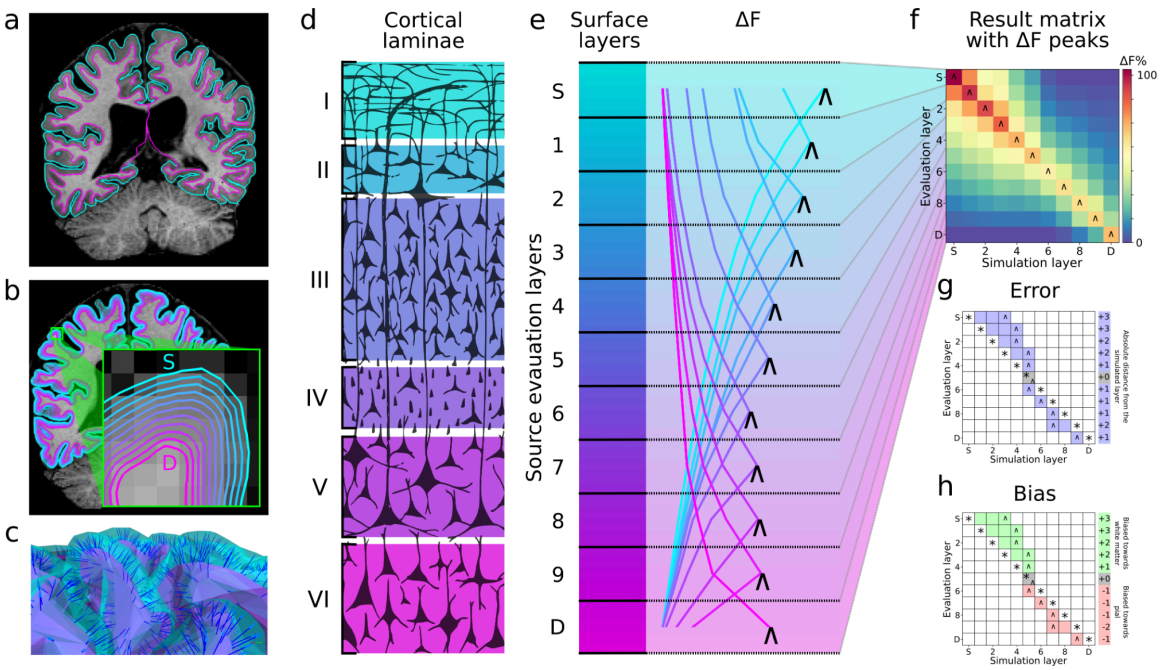

Figure 1. Overview of the simulation strategy and analysis. a) Pial and white matter boundaries surfaces are extracted from anatomical MRI volumes. **b)** Intermediate equidistant surfaces are generated between the pial and white matter surfaces (labeled as superficial (S) and deep (D) respectively). **c)** Surfaces are downsampled together, maintaining vertex correspondence across layers. Dipole orientations are constrained using vectors linking corresponding vertices (link vectors). **d)** The thickness of cortical laminae varies across the cortical depth (*70*–*72*), which is evenly sampled by the equidistant source surface layers. **e)** Each colored line represents the model evidence (relative

to the worst model, ΔF) over source layer models, for a signal simulated at a particular layer (the simulated layer is indicated by the line color). The source layer model with the maximal ΔF is indicated by "^". **f)** Result matrix summarizing ΔF across simulated source locations, with peak relative model evidence marked with "^". **g)** Error is calculated from the result matrix as the absolute distance in mm or layers from the simulated source (*) to the peak ΔF (^). **h)** Bias is calculated as the relative position of the peak ΔF(^) to the simulated source (*) in layers or mm.

Analysis

For each simulated dataset, we applied multiple sparse priors (MSP) inversion (*73*) to each simulated dataset within a Hann windowed 50 ms analysis window centered around the peak of the simulated Gaussian temporal profile. These data were projected into 274 orthogonal spatial modes and 4 temporal modes, with a patch size of 5 mm (unless otherwise specified) and a single prior corresponding to the vertex the activity was simulated at. This was done to test the feasibility of a sliding time window approach previously applied to bilaminar MEG dynamics (Bonaiuto et al., 2021). Because each time window is evaluated independently in this framework, a single 50 ms window was sufficient for our analysis. We confirmed the robustness of this window size in supplementary simulations testing 15, 25, 50, and 100 ms windows (Figure S1), which showed consistent reconstruction performance across a broad temporal range. Rather than performing source reconstruction on a single multilayer cortical mesh, we conducted separate MSP inversions for each of the 11 cortical depth surfaces, treating each as an independent forward model. For each simulation, we computed the model evidence (free energy) for each depth-specific source reconstruction and identified the cortical surface with the highest model evidence (Figure 1e). This allowed us to infer the most likely depth of the simulated source by comparing the relative free energy across reconstructions at different cortical depths (Figure 1f).

We quantified reconstruction accuracy by identifying the surface with the highest model evidence and comparing its depth to the known simulated source depth. Reconstruction error was computed as the absolute difference between the simulated and inferred depths (Figure 1g), measured both in number of surfaces and in millimeters by scaling surface indices using local cortical thickness. Reconstruction bias was defined as the signed difference between simulated and inferred depths (Figure 1h). To assess statistical significance, we performed permutation tests using 10,000 iterations, shuffling the free energy matrices for each simulated cortical depth and recomputing error and bias distributions under the null hypothesis of no depth sensitivity. P-values were calculated by comparing observed reconstruction errors and biases against these shuffled distributions, with statistical significance determined at $p < 0.05$. Effect sizes were computed using Cohen's d, defined as the difference between observed and shuffled means divided by the standard deviation of the shuffled distribution. We conducted bootstrap resampling (5,000 iterations), drawing random subsets of the data to compute 95% confidence intervals for error and bias. We also computed a diagonal dominance score to quantify the extent to which model evidence matrices favored reconstructions at the correct depth. This score, representing the ratio of diagonal values to total values in the free energy matrix, was compared against a permuted distribution (N = 10,000) to assess whether observed diagonality exceeded chance levels.

We accounted for cortical laminae thickness variability by incorporating the BigBrain atlas (*74*, *75*). Because cortical laminae differ in thickness across the brain (Figure 1d), mapping simulated and inferred sources to cytoarchitectonic laminae rather than fixed-depth surfaces improves biological interpretability. To achieve this, we mapped the BigBrain atlas to the subject's anatomy via FreeSurfer's surface-based registration through *fsaverage* space (*76*). This allowed us to align the proportional cortical laminae boundaries from the atlas with the subject's individual cortical geometry. For each simulated cortical location, we extracted the proportional laminae boundaries (six depth values defining the transitions between laminae) using precomputed laminar thickness estimates from the atlas. These boundaries were then scaled by the local cortical thickness to derive laminar depths in millimeters. The final mapping step assigned each of the 11 cortical surface layers used for source reconstruction to a corresponding cytoarchitectonic laminae. Reconstruction errors were then computed in laminar space rather than in fixed surface coordinates; specifically, an inferred source depth was only considered an error if it fell outside the lamina of the simulated source, regardless of its precise position in cortical depth. Significance was evaluated using the same permutation-based approach used for error in terms of layers and millimeters (N = 10,000).

To evaluate how local anatomy influences laminar inference, we quantified reconstruction error at each cortical location and related it to anatomical features. For each vertex, we computed absolute reconstruction error in millimeters. We then analyzed the relationship between reconstruction error and several anatomical properties: cortical thickness (measured between the pial and white matter surfaces), distance to the scalp surface, orientation of the cortical column relative to the scalp, and variability in lead field magnitude across depth. Orientation was computed as the absolute dot product between the simulated dipole orientation and the scalp normal at each vertex. Lead field variability was quantified as the root mean square difference in lead field magnitude across surface layers, relative to the superficial (pial) surface. These features were then related to reconstruction error using kernel density estimation and receiver operating characteristic (ROC) analysis to identify anatomical thresholds predictive of accurate inference. To assess whether anatomical features jointly predict laminar inference accuracy better than single features, we performed multivariate logistic regression and random forest classification. We evaluated model performance using 5-fold cross-validated ROC analysis. Logistic regression models were tested both with and without pairwise interaction terms to quantify potential nonlinear feature interactions. Random forest hyperparameters were set to 500 trees, unlimited depth, balanced class weights, and a fixed random seed for reproducibility.

Results

SNR-dependent patterns of laminar inference accuracy

To determine the SNR required for accurate laminar reconstruction across multiple cortical depths, we selected 100 random cortical locations (vertices on the pial surface). At each location, we ran 11 simulations, each simulating a source signal with a Gaussian temporal profile at the corresponding vertex on one of 11 surface meshes ranging from the white matter (deepest) to pial (most superficial) surface (see Figure S1 for simulated time-course). For each simulation, we ran source reconstruction (MSP, with the prior set to the simulated cortical location) within a 50 ms central window 11 times, each time using a different surface mesh to construct the forward model, and compared the resulting model evidence, approximated by free energy. In the absence of noise (e.g. sensor noise, co-registration

error etc), the model based on the surface corresponding to the depth of the simulated signal will have greater model evidence, or free energy (i.e. if a signal is simulated on the pial surface, the model based on the pial surface should have the greatest free energy). This set of simulations was repeated at each selected cortical location with different levels of simulated sensor-level SNR, varying from -∞ (pure noise) to 5 dB.

For each location, this yielded a matrix of model evidence (free energy) with a column for simulation at each cortical depth, and a row for each forward model. For each simulated cortical depth (matrix column), we transformed free energy values for each forward model by subtracting the lowest value, thus representing model evidence relative to the worst model. For each matrix, we identified the model with the peak free energy for each simulated cortical depth, and generated a probability density of these peaks for each SNR level. We also computed a measure of diagonal dominance, or the ratio of diagonal values to total values (perfect laminar reconstruction would yield a purely diagonal matrix), and compared this to a null distribution obtained by shuffling the matrices. At low levels of SNR (< -50 dB), there was no pattern in the mean free energy (averaged over all simulated locations) over simulated cortical depths (Figure 2a). However, the probability density of surfaces with the maximal free energy demonstrates that in most locations, the peak free energy corresponded to either the most superficial or the deepest surface model (Figure 2e). At -50 dB, a step change in the mean free energy was observed, with the greatest mean free energy for roughly the surface corresponding to the simulated depth (Figure 2b), and a diagonal dominance score greater than expected by chance (d = 3.22, p = 0.001; Figure S2a). A corresponding gradient in the probability density of the peak free energy model was observed, with a greater probability for superficial surface model peaks for superficial simulations, and for deep surface model peaks for deep simulations (Figure 2f). At higher levels of SNR (≥- 35 dB), both the mean free energy (Figure 2c,d) and the probability density (Figure 2g,h) exhibited significant diagonality (all d > 3.5, all p < 0.001; Figure S2a), indicating near perfect inference of the depth of the simulated signal.

At each cortical location, we computed bias as the mean distance, over the 11 simulations, between the simulated source and the surface model with the highest free energy (in terms of surfaces and millimeters), and error as the mean absolute distance between the simulated surface and the best surface models (also in surfaces and millimeters). For each metric, we compared the observed values across simulated SNR levels with the null distribution obtained by shuffling the surface model free energy for each simulated depth. At low SNR levels (-50 dB and below), both error and bias were at chance levels (p > 0.05 and p > 0.8, respectively). A significant reduction in error emerged at -35 dB (d = -4.17, p < 0.001), with further minimal error at -20 dB and above (all d > 4.8, all p < 0.001; Figure 2i,j). Bias was not significant at any SNR level (all p > 0.8), though extreme deep or superficial biases were observed at some locations below -50 dB (Figure 2k,l). These results were nearly identical when error and bias were computed in millimeters rather than surface layers (Figure 2k,l). Consistent with previous simulation results (*53*), inference was biased at low SNR levels when using the empirical Bayesian beamformer algorithm (Figure S3) (EBB; *77*, *78*) rather than MSP with a spatial prior, as used in this study. We also examined error separately for each simulated surface layer and found no differences between layers (Figure S4a). Laminar inference at a coarse scale (deep versus superficial) is therefore possible in principle at -50 to -35 dB SNR, with fine-scale inference possible at -20 dB and above.

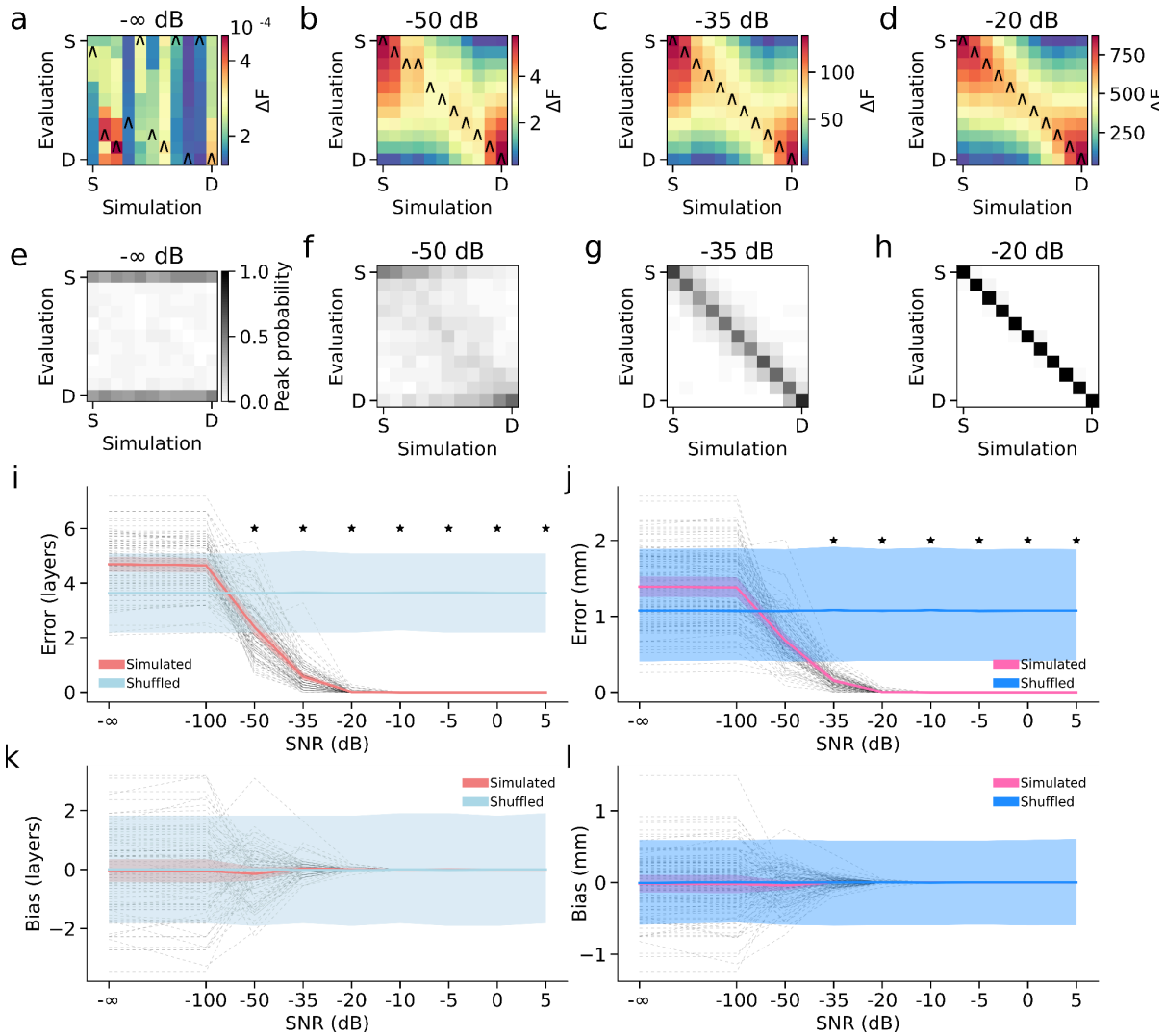

Figure 2. Laminar source-reconstruction accuracy as a function of sensor-level SNR. a–d) Mean model evidence (free energy, ΔF) matrices (row-normalized to the worst model; S = superficial surface layer, D = deep surface layer) for simulated signals placed on 11 cortical surfaces at four SNR levels (−∞ dB, −50 dB, −35 dB, −20 dB). Accurate laminar inference begins to emerge around –35 dB (**c**), with near-perfect identification at –20 dB (**d**). Triangular markers denote the forward model with peak free energy for each simulated depth. **e–h)** Probability density of each forward model being the maximum-evidence solution, aggregated across cortical locations: a diagonal pattern appears from –35 dB, indicating accurate depth localization. **i, j)** Laminar reconstruction error (in layers and mm) falls below chance at –35 dB and improves at higher SNR; shuffled controls show ~1 mm error due to chance matches between simulated and evaluated layers. **k, l)** Laminar reconstruction bias (in surface layers and millimeters), again comparing simulated and shuffled data. Shaded bands represent 95% confidence intervals, and asterisks mark SNR levels at which observed error or bias differed significantly from chance ($p < 0.05$).

Impact of co-registration error on laminar inference

Previous work suggests that accurate laminar inference is feasible with up to 2 mm of co-registration error (*52*, *53*). To evaluate whether this holds in our multilayer framework, we ran another set of similar simulations at the same cortical locations, this time fixing the SNR at 0 dB, and varying the simulated co-registration error from 0 to 5 mm. At levels of co-registration less than or equal to 2 mm, the surface model with the highest mean free energy corresponded to the simulated cortical depth (Figure 3a-c), and the peak free energy model probability density exhibited strong diagonality (all $d > 4$, all $p < 0.001$: Figure 3e-f;

Figure S2b), indicating accurate inference across the range of simulated depths. At higher levels of co-registration error (3-5 mm), the mean free energy still exhibited significant diagonality (all $d > 3.9$, all $p < 0.001$; Figure 3d; Figure S2b), but the probability density only indicated a gradient in free energy peaks in the deepest and most superficial surfaces (Figure 3h).

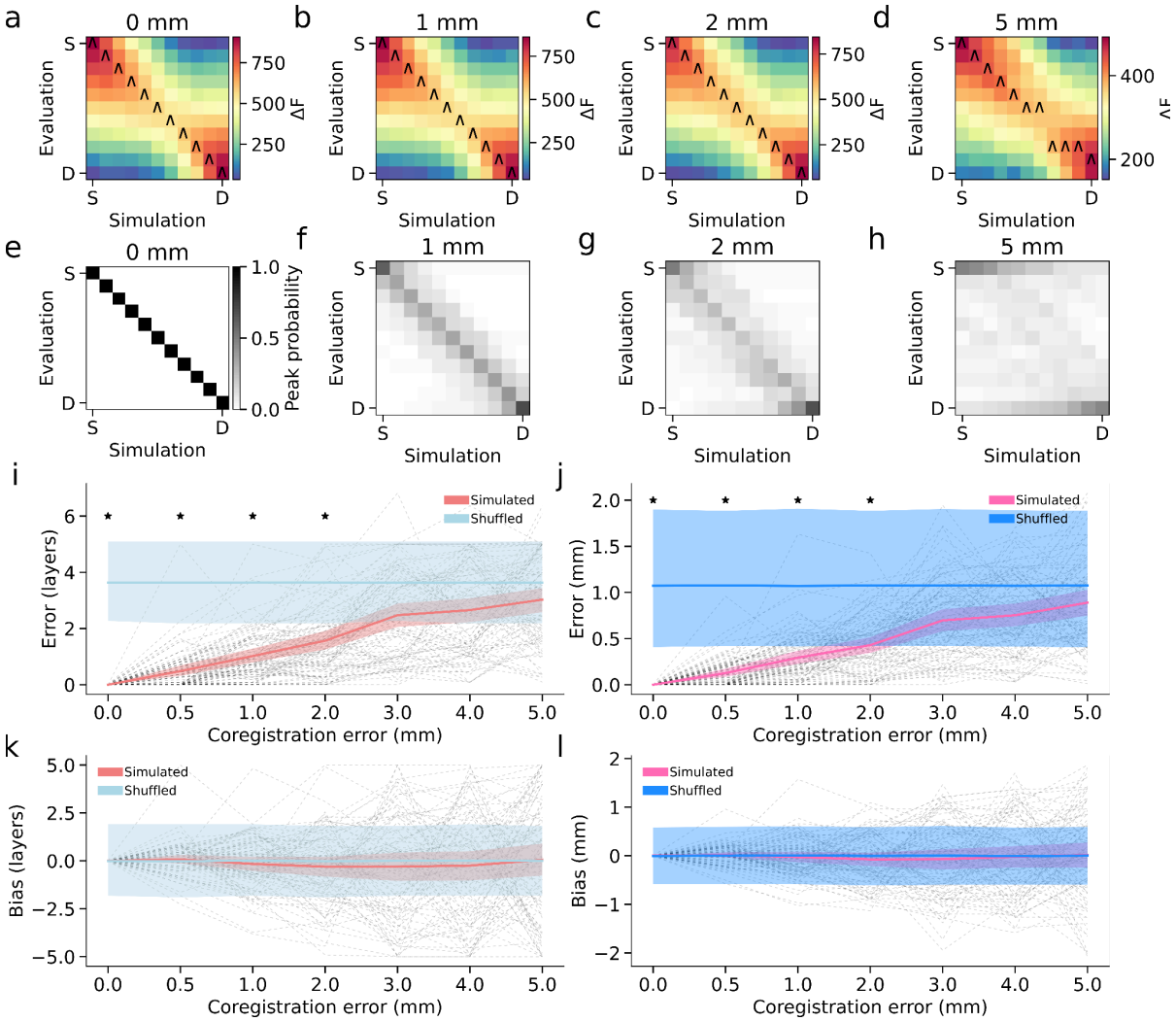

Figure 3. Laminar source-reconstruction accuracy as a function of co-registration error at fixed 0 dB SNR. a–d) Mean free energy (ΔF) matrices (row-normalized to the worst model; S = superficial surface layer, D = deep surface layer) for simulated signals placed on 11 cortical surfaces at 0, 1, 2, and 5 mm registration error. Triangles mark the best-fitting forward model for each simulated depth. **e–h)** Probability density of each surface model being the maximum-evidence solution, aggregated across cortical locations. **i, j)** Laminar reconstruction error (in surface layers and millimeters) for simulated versus shuffled data at varying registration errors. **k, l)** Corresponding bias (in surface layers and millimeters). Shaded bands denote 95% confidence intervals, and asterisks mark significance at $p < 0.05$.

We computed bias and error for the co-registration error simulations using the same approach as in the SNR simulations and compared the observed values against the null distribution obtained by shuffling. Error was lowest at 0 mm (d = -4.84, $p < 0.001$) and progressively increased with greater co-registration error, though it remained significantly lower than chance levels up to 2 mm (d = -2.77, p = 0.002; Figure 3i,j). At 3 mm and above, error was at chance level (all $p > 0.06$). There was no significant bias at any level of co-registration error (all $p > 0.7$). These results were nearly identical when error and bias

were computed in millimeters rather than surface layers (Figure 3k,l). When split by simulated surface layer, the accuracy of laminar inference for simulated deep sources was less affected by coregistration error than superficial sources (Figure S4b). Accurate laminar inference therefore requires a co-registration error of 2 mm or less, though a coarse deep-versus-superficial distinction may be possible in some locations at errors up to 5 mm, provided there is sufficient SNR.

SNR and co-registration error required for true laminar inference

Given that cortical laminae vary in thickness both within and across regions (*70*–*72*), we assessed laminar reconstruction accuracy in terms of cytoarchitectonic laminae rather than fixed-depth surfaces. Specifically, surface layers that mapped to the same lamina were treated as equivalent (e.g., errors between adjacent surface layers were not considered errors if both corresponded to lamina VI). To achieve this, we re-analyzed the effects of SNR and co-registration error using the BigBrain atlas (*74*, *75*), which we mapped to the subject's anatomy via FreeSurfer's surface-based registration through *fsaverage* space (*76*). This allowed us to estimate proportional laminar thickness at each simulated cortical location (Figure 4a-f), assign surface layers to their corresponding laminae, and evaluate reconstruction accuracy in terms of cytoarchitectonic rather than geometric depth.

We re-analyzed both SNR and co-registration error simulations under this framework. Error was computed as the absolute difference between the simulated and inferred lamina, and significance was assessed using permutation tests (N = 10,000) against a shuffled null distribution. At very low SNR levels (-100 dB and below), reconstruction error was indistinguishable from chance for all laminae (all $p > 0.8$). At -50 dB, inference remained at chance for middle laminae (laminae III and IV; both $p > 0.07$) but was significantly better than chance for superficial and deep laminae (all $p < 0.001$). By -35 dB, reconstruction accuracy improved across all laminae (all $p < 0.001$), with effect sizes ranging from $d = -11.36$ to $d = -23.15$ (Figure 4g). The most pronounced improvements were observed at -20 dB and above, where errors reached minimal levels (all $d < -14.57$, all $p < 0.001$). These results confirm that true laminar inference is possible at sufficiently high SNR, even when accounting for regional variability in cortical layer thickness.

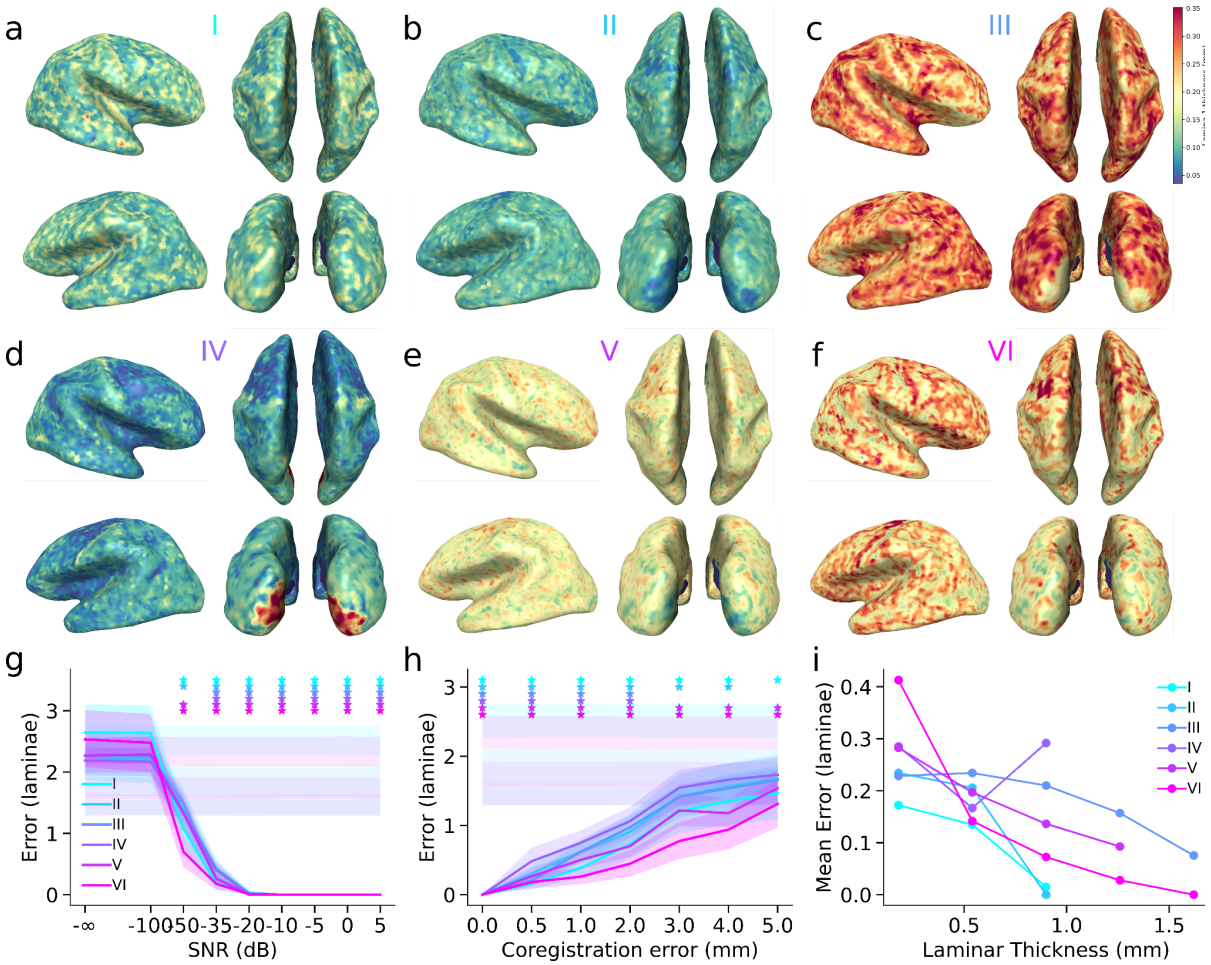

Figure 4. Laminar source-reconstruction accuracy as a function of SNR, co-registration error, and cortical thickness. a–f) Cortical surfaces showing laminar thickness across the brain, derived from the BigBrain atlas and mapped onto the surface models (representing laminae I-VI respectively) used in the simulations. These maps illustrate the variability of laminar thickness across cortical regions, which influences inference accuracy. **g)** Mean laminar reconstruction error (in laminae) across SNR levels, computed as the absolute difference between the simulated and inferred lamina. Lines indicate the mean error for each lamina, with shaded bands representing 95% confidence intervals. Lighter shaded bands represent shuffled null distributions. Asterisks mark SNR levels where reconstruction error was significantly lower than chance. **h)** Mean laminar reconstruction error as a function of co-registration error. **i)** Relationship between laminar thickness and reconstruction error. Each line represents a different lamina (I–VI), showing how increased laminar thickness is associated with reduced reconstruction error.

Co-registration errors had a similar impact, with small misalignment (≤ 2 mm) having minimal effects on reconstruction accuracy across all laminae (all $p < 0.001$), while increasing error progressively degraded performance. At 2 mm, reconstruction accuracy remained high (all $d < -4.45$, all $p < 0.001$), but at 3 and 4 mm, performance declined sharply, particularly for middle laminae (laminae III and IV; both $p > 0.4$; Figure 4h). At 5 mm, only the most superficial (lamina I) and deepest laminae (laminae V and VI) remained significantly different from chance (lamina I: $d = -8.51$, $p < 0.001$; lamina V: $d = -2.10$, $p = 0.018$; lamina VI: $d = -8.45$, $p < 0.001$). These findings suggest that fine-scale laminar inference is robust to small co-registration errors but becomes unreliable at misalignment exceeding ~3 mm, particularly for middle-layer sources. At errors of 5 mm, only deep and superficial sources retain some discriminability, indicating that accurate reconstruction at this scale requires co-registration precision within at least approximately 2 mm.

Finally, we assessed how laminar reconstruction accuracy depends on laminar thickness, focusing on the results of simulations with SNR of at least -20 dB and co-registration errors less than or equal to 2 mm. Across simulated locations, thicker laminae exhibited systematically lower reconstruction error (Figure 4i), reflecting a greater spatial margin for accurate depth localization. This effect was most pronounced in deep and superficial laminae, where increased cortical thickness improved inference reliability. Middle laminae, in contrast, showed greater variability in error, consistent with the higher misclassification rates observed at moderate SNR and co-registration error levels. Cortical laminae thickness therefore impacts laminar reconstruction accuracy, with thicker laminae providing a greater margin for accurate depth localization. The increased variability in middle laminae suggests that reconstruction accuracy is not uniform across the cortex, requiring inference strategies that consider regional differences in laminar architecture.

Limitations of laminar inference for multiple simultaneous sources

Having established that a single source can be accurately localized in depth given sufficient SNR and co-registration accuracy, we next examined whether two simultaneous sources of equal strength at different layers could be differentiated. To test this, we simulated two sources at each of the 100 cortical locations: one fixed in the middle layer and the other varying from the most superficial to the deepest layer surface (SNR = -20 dB, co-registration error = 0 mm). Across all simulations, rather than producing two distinct peaks in relative model evidence, a single peak consistently emerged at an intermediate depth between the two sources, both in mean free energy (Figure 5a) and in the peak free energy model probability density (Figure 5b). This suggests that the presence of the middle-layer source systematically biased laminar inference toward the middle-layer model compared to single-source simulations (Figure 5e,f). However, further analysis of the free energy distribution across models (Figure 5c) and across simulations (Figure 5d) suggests that distinct contributions from both sources may still be present. Notably, model evidence for the middle-layer surface was higher relative to single-source simulations (Figure 5g,h), indicating that while the current approach does not fully resolve two simultaneous sources, further refinement of the method may improve discriminability.

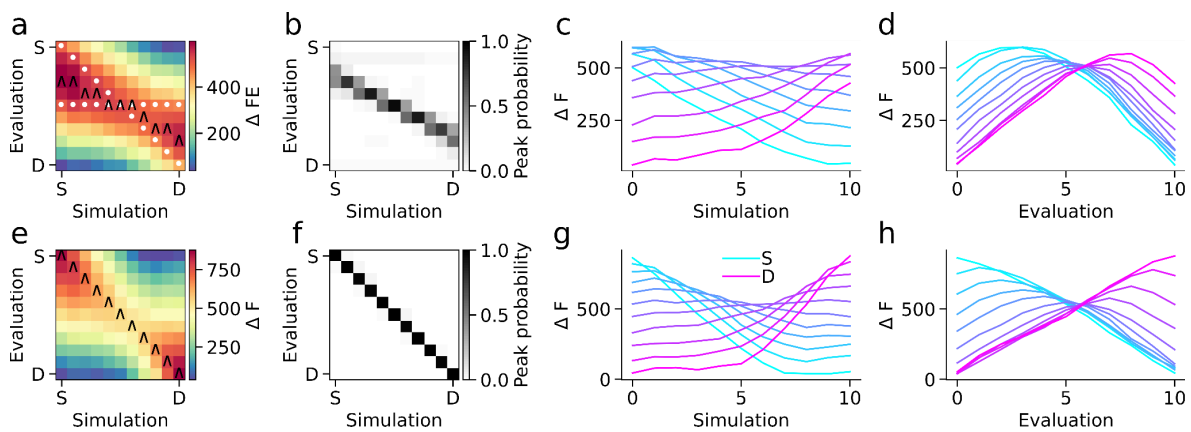

Figure 5. Two-source simulations at −20 dB SNR highlight the difficulty of separating simultaneous laminar sources. a,b) When one source was fixed at the middle layer and a second source was varied from superficial to deep, the mean free-energy (ΔF) matrices and peak-probability plots showed a single intermediate peak, indicating bias toward the middle-layer model (S = superficial surface layer, D = deep surface layer). **c,d)** Despite this bias, plots of ΔF across simulated layers (c) and across forward-model evaluations (d) reveal that deeper and more superficial

contributions still influence the model evidence. **e–h)** In contrast, single-source simulations at the same SNR showed stronger diagonality in ΔF (e,f) and clearer separation in layer-by-layer analyses (g,h), suggesting that additional refinements are needed to fully disentangle two concurrent laminar sources.

Cortical column orientation estimation influences laminar inference accuracy

We assessed the influence of dipole orientation estimation on laminar source reconstruction by evaluating four methods (*61*): surface normals from the original high-resolution mesh (OSN), surface normals from the downsampled mesh (DSN; *65–68*), cortical patch statistics (CPS; *69*), and link vectors (LV) computed between corresponding vertices on the pial and white matter surfaces (*60*). For each method except link vectors, we included variants with orientations fixed across layers ("fixed") and orientations independently computed per layer (link vectors have the same orientation at corresponding vertices across surfaces by definition). This resulted in seven variations in dipole orientation definition. Figure 6a illustrates these methods applied across cortical depth at representative vertices.

To quantify differences between orientation vectors, we computed the angular deviation between each pair of methods at each cortical depth. These deviations were highest between LV and surface-normal-based approaches (Figure 6c–e). The fixed variants of the surface-normal-based approaches used the surface normals computed from the pial surface, and therefore the angular deviation between fixed and non-fixed variants of the same family increased with cortical depth (Figure 6c-e). We then tested how these orientation discrepancies affected reconstruction performance by simulating laminar sources using each method and reconstructing them with each of the others. Reconstruction error, defined as the deviation between the inferred and ground truth layer, was lowest when the same method was used for both simulation and reconstruction (Figure 6f–h), consistent with prior findings (*61*). Errors were highest when simulation and reconstruction orientations were mismatched, particularly across different estimation families (e.g., LV vs DSN).

Across cortical depths, we observed a strong positive and nonlinear relationship between angular discrepancies in dipole orientation and errors in laminar source reconstruction (Figure 6b), indicating that even modest orientation misalignment can degrade depth precision. Importantly, we found no consistent advantage for fixed-orientation strategies over those allowing depth-varying orientations, suggesting that anatomical consistency across layers is less critical than aligning dipole orientations with the true cortical column geometry. These results underscore the importance of accurately estimating dipole orientation when performing laminar inference in real data, and caution against using anatomically implausible orientation models.

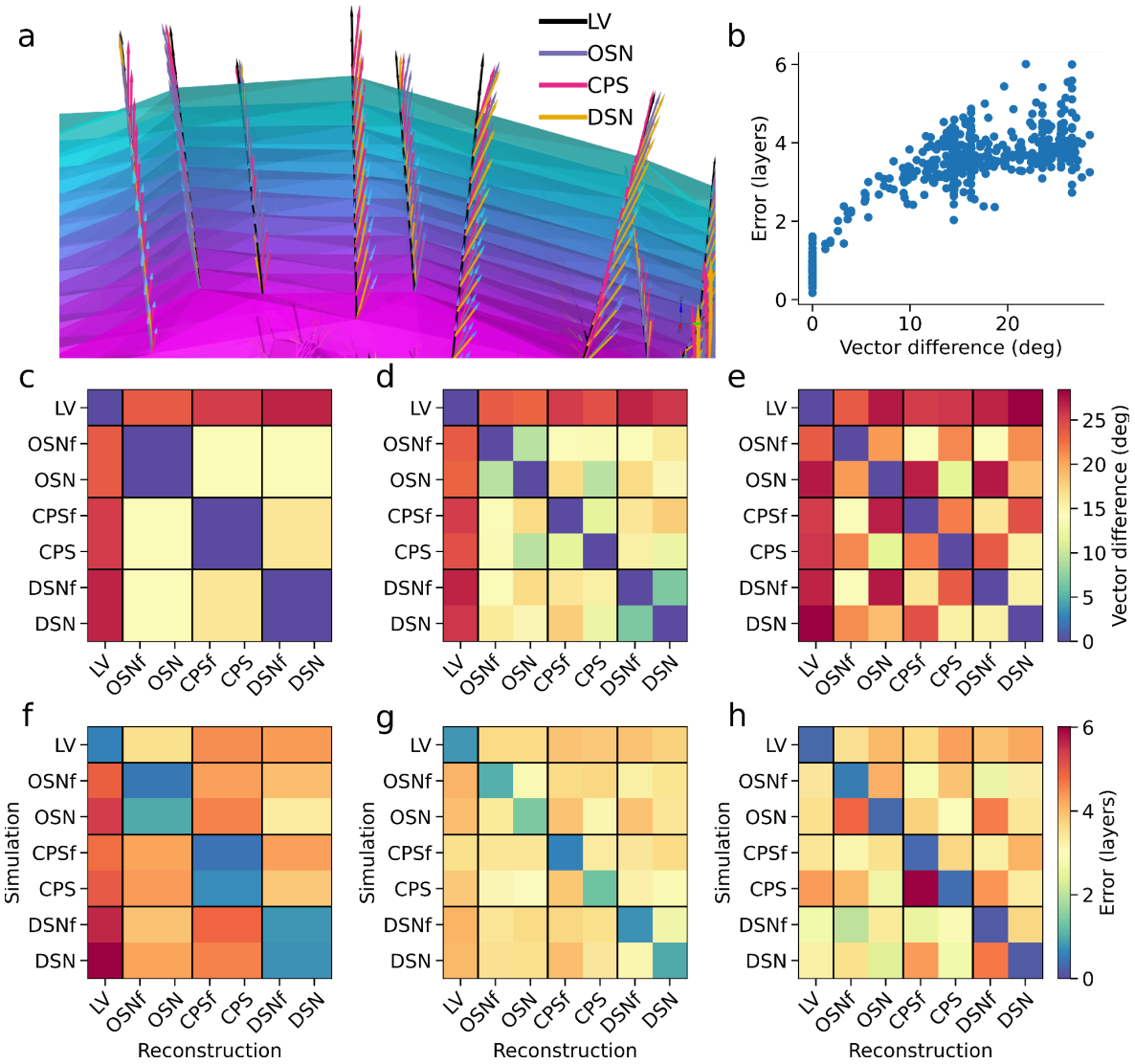

Figure 6. Impact of dipole orientation estimation on laminar source reconstruction accuracy. **a)** Example dipole orientation vectors at a subset of cortical locations across layers for four methods: link vectors (LV), original surface normals (OSN), cortical patch statistics (CPS), and downsampled surface normals (DSN). **b)** Relationship between orientation mismatch (angular difference in degrees) and laminar reconstruction error, over all simulation–reconstruction method pairs and cortical depths. **c–e)** Angular deviation (median across vertices) between orientation estimation methods at three cortical depths: superficial (**c**, surface layer 1), middle (**d**, surface layer 6), and deep (**e**, surface layer 11). **f–h)** Corresponding reconstruction error (in layers) for each simulation–reconstruction method pair at the same depths, averaged across 100 cortical locations. Errors are lowest along the diagonal, where simulation and reconstruction methods match, and largest when methods differ substantially (LV – link vectors; OSN – original surface normals; CPS – cortical patch statistics; DSN – downsampled surface normals. The suffix "f" indicates dipole orientations were fixed across layers).

Anatomical features determine the accuracy of laminar inference

The previous analyses demonstrate that laminar inference accuracy critically depends on signal quality, co-registration precision, and accurate estimates of cortical column orientation. However, even with optimal signal-to-noise ratio (≥ –20 dB) and zero co-registration error, reconstruction accuracy is not uniform across the cortex (*53*). This variability suggests that local anatomical properties may impose inherent constraints on laminar reconstruction. To evaluate how anatomical variability influences laminar source

reconstruction, we simulated, one at a time, sources at every vertex of a multilayer cortical mesh (29,130 locations × 11 layers) under these idealized conditions. Laminar depth was inferred using model evidence across all cortical layers. Reconstruction error, defined as the absolute difference between the simulated and inferred depth, was zero for 24,699 out of 29,130 vertices (84.79%), indicating that laminar inference is feasible across most of the cortex under these conditions. However, reconstruction accuracy varied regionally, with errors concentrated in anatomically constrained areas (Figure 7a).

To understand the anatomical basis for this regional variation, we examined four candidate factors: lead field separation between deep and superficial layers (Figure 7b), dipole orientation relative to the scalp (Figure 7c), scalp–cortex distance (Figure 7e), and cortical thickness (Figure 7g). Although none of these features perfectly separated vertices with zero error from those with nonzero error, all were significantly associated with reconstruction error. Specifically, vertices with low laminar discriminability exhibited smaller lead field differences between depths, more tangential orientations, greater distances from sensors, and thinner cortices.

Joint density plots and marginal histograms revealed that these relationships were nonlinear (Figure 7d,f,h). Among all features, the dissimilarity between deep and superficial lead fields emerged as the strongest predictor of error (optimal threshold = 0.09 a.u.; AUC = 0.756), suggesting that the ability to distinguish layer-specific contributions at the sensor level places a fundamental constraint on laminar inference. Cortical thickness (optimal threshold = 2.91 mm; AUC = 0.749) and scalp distance (optimal threshold = 24.43 mm; AUC = 0.689) also contributed, consistent with prior work on MEG sensitivity profiles, whereas dipole orientation had a weaker but still detectable effect (optimal threshold = 0.71 a.u.; AUC = 0.595). These findings suggest that even under favorable conditions, anatomical constraints shape the spatial distribution of inference precision.

To determine whether combinations of anatomical features better predict laminar inference accuracy than single features, we performed a multivariate logistic regression analysis. The logistic regression model significantly discriminated between error-free and erroneous reconstructions (mean cross-validated AUC = 0.810 ± 0.013), with the largest positive coefficient assigned to lead field difference (β = 10.64), followed by orientation relative to the scalp (β = 1.01) and cortical thickness (β = 0.76); scalp–cortex distance had minimal influence (β = –0.02). Adding pairwise interaction terms provided only a negligible improvement (mean cross-validated AUC = 0.812 ± 0.015). A random forest classifier corroborated these findings, highlighting the lead field difference as the strongest predictor (importance = 32%), followed by thickness (27%), distance (22%), and orientation (19%), though it did not enhance prediction accuracy beyond logistic regression (mean cross-validated AUC = 0.804 ± 0.013). Together, these results indicate that anatomical constraints on laminar inference accuracy primarily arise from additive contributions of distinct features rather than from complex interactions.

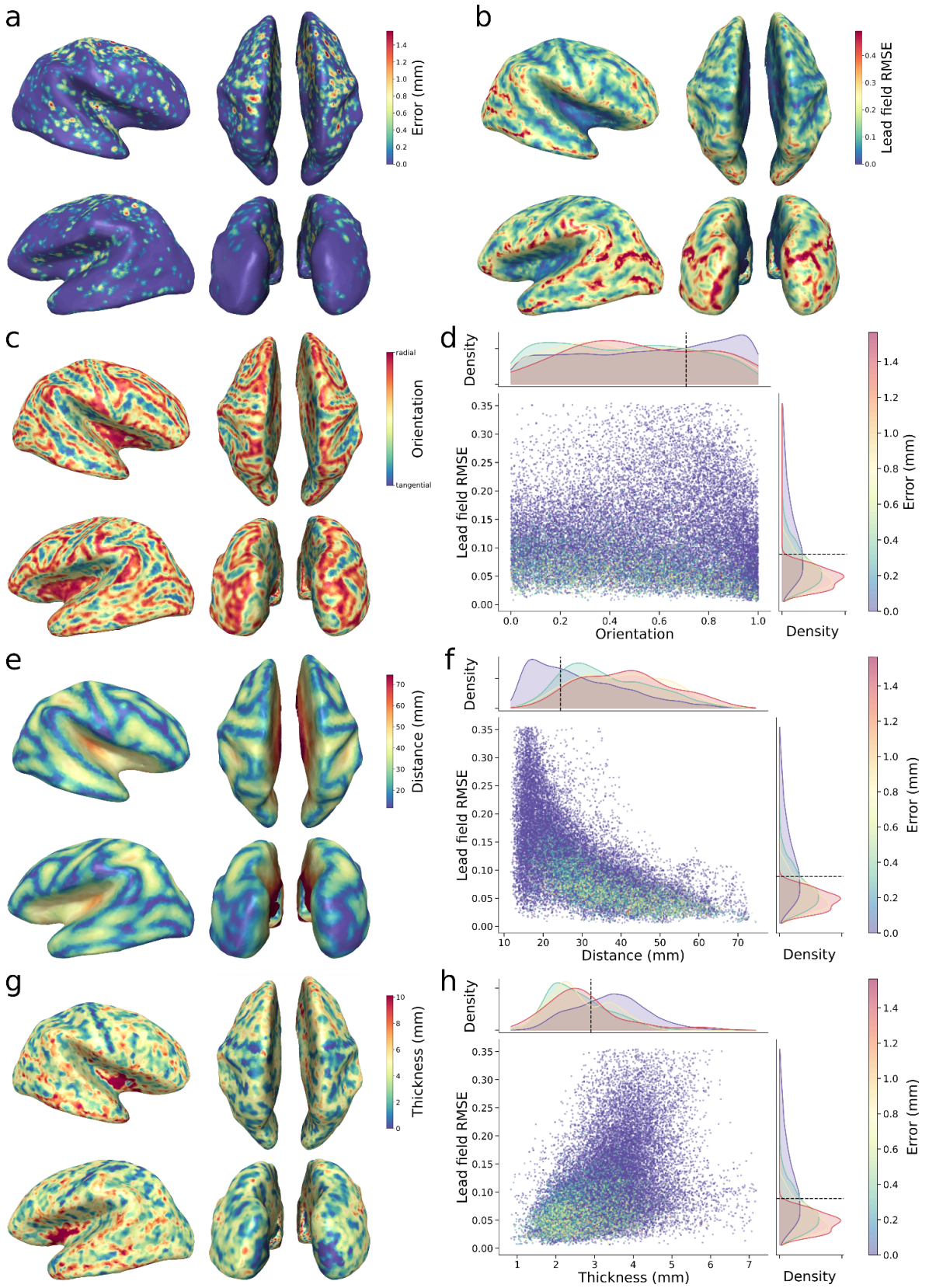

Figure 7. Anatomical factors influencing laminar reconstruction error. a-b) Inflated-surface maps of laminar reconstruction error (a) and lead-field RMSE (deep vs. superficial; b) **c-h**) Inflated-surface maps and joint density and marginal histograms for each anatomical metric versus lead-field RMSE: and dipole orientation (c,d), scalp–cortex distance (e,f), and cortical thickness (g-h). Joint density plots are color-coded by laminar reconstruction error (mm). Lower lead-field differences,

tangential orientations, greater distance to the scalp, and thinner cortex are associated with increased laminar-reconstruction error.

Discussion

Building upon previous bilaminar models of laminar inference in high-precision MEG (hpMEG), we introduce a multilayer source reconstruction framework that enables depth-resolved inference across the full cortical column. Our simulations reveal that this precision requires a sufficiently high signal-to-noise ratio (approximately -35 dB for bilaminar and -20 dB for full laminar inference) and minimal co-registration error (< 2mm), conditions that can be met in practice through the use of individualized head-casts and optimized recording protocols (*54*, *55*). Although coarse deep-versus-superficial distinctions remain feasible at lower SNRs with two-layer source models, true six-laminar resolution requires fine-grained depth coverage to account for variations in laminar thickness across the cortex. Crucially, we confirm that correctly estimating cortical column orientation is essential for accurate laminar inference, as errors in dipole orientation estimation systematically degrade localization accuracy. Corroborating previously established results (*53*), we show that anatomical features of the cortex such as thickness, dipole orientation, scalp–cortex distance, and lead field separation across depths nonlinearly shape the spatial distribution of inference accuracy, with lead field dissimilarity emerging as the strongest predictor.

Despite the significant improvements offered by our multilayer approach, a key limitation is the inability of current model-based inference methods to resolve two simultaneous sources of equal magnitude at different depths. While exact temporal alignment and perfectly matched dipole moments are unlikely in biological systems, this limitation highlights the constraints of relying solely on Bayesian model comparison. Specifically, two closely spaced dipoles at different depths may generate a sensor-level field pattern indistinguishable from a single intermediate dipole, limiting the spatial discrimination achievable by current MEG systems. One potential solution would be to use sensors capable of measuring higher spatial-frequency components of the magnetic fields, such as optically pumped magnetometers (OPMs), which could increase sensitivity to subtle spatial differences between closely spaced sources (*79*–*81*). Future refinements should explore both sensor technology advances and alternative inference strategies, such as Bayesian model averaging (BMA), which assigns probabilistic weights to multiple competing models rather than selecting a single best-fit model (*82*, *83*). These combined approaches may enhance the simultaneous resolution of multiple sources, overcoming a fundamental limitation of the current winner-takes-all approach.

A related consideration is the spatial extent of the generative source. In additional simulations, we simulated 5 mm patches of cortical activity and assessed reconstruction performance using source models with varying patch sizes (2.5 mm, 5 mm, and 10 mm FWHM). We found that mismatches between the true patch size and the extent assumed in the generative model systematically biased reconstruction: underestimation led to deeper solutions, whereas overestimation biased inference toward superficial layers (Figure S5). These results align with prior findings (*52*, *53*), and reinforce the importance of accurate assumptions about the spatial spread of the source, which could vary between laminae and depends on factors such as lateral cortical connectivity.

In supplementary simulations using different sliding window sizes (15, 25, 50, and 100 ms; Figure S1), we assessed the temporal sensitivity of laminar model evidence. Across all window lengths, model-based inference consistently recovered the true laminar depth, but the temporal profile of model evidence differed. Narrow windows (e.g., 15 ms) yielded sharper by noisier evidence profiles that collapsed earlier, while wider windows (e.g., 100 ms) integrated more information, resulting in broader and more stable evidence plateaus over time. This trade-off reflects the balance between temporal resolution and sensitivity: short windows enable finer tracking of rapid changes but require high SNR, whereas longer windows are more robust to noise but may obscure transient laminar dynamics.

As demonstrated above, model-based laminar inference requires careful selection of parameters and prior models. A more direct, though equally technically challenging, approach would be to extract source signals directly from each surface layer model rather than relying on model-based inference. This might resemble laminar local field potential (LFP) recordings and could, in principle, enable direct current source density (CSD) estimation. However, even laminar LFP recordings are extracellular and thus remain subject to an inverse problem due to aggregation of diverse signal sources (*84*), that is typically ignored in conventional CSD analyses (*29*). Consequently, applying CSD-like methods (e.g. *85–88*) to hpMEG presents significant challenges, including sign ambiguity (*89*) and sensitivity to noise (*90*). Additionally, MEG signals integrate across a broader neural population than LFPs, further complicating their interpretation (*91*). Without concurrent intracranial validation, direct hpMEG-based laminar signal extraction remains an open challenge. Depth-resolved source reconstructions are most amenable to empirical validation in contexts where laminar activation patterns are well-characterized from invasive studies such as sensory or motor event-related responses, making them ideal test cases for evaluating hpMEG accuracy. Validating hpMEG in these domains would enable generalization of laminar inference to non-invasive studies of cognition and pathology, where invasive ground truth is not available. Future studies could achieve this by integrating hpMEG with intracortical recordings in animals or rare human datasets (*26*).

A practical consideration for real-world applications is the effect of dynamic head motion on co-registration error. In our simulations, co-registration error was modeled as static for computational efficiency, but in real recordings, even small head movements may introduce depth-localization errors. The most effective way to mitigate motion is through individualized head-casts, which substantially reduce head displacement and can realistically achieve < 2 mm coregistration error (*54*, *55*). Alternatively, wearable customized arrays of OPMs could achieve similar precision by moving with the head, thus inherently reducing motion-induced errors (*92*, *93*). While head-casts or wearable OPM arrays do not eliminate movement entirely, residual movement artifacts can be addressed using additional correction strategies, including regression of motion-related signals (*94*, *95*) or temporally extended source space separation (tSSS), which virtually transforms the sensor array to move with the head (*96*, *97*). Combining physical stabilization with signal-level correction may be necessary to reach the precision required for robust laminar inference in practice.

The ability to resolve sources with laminar precision necessitates a reevaluation of the theoretical limits of MEG resolution. The estimated number of pyramidal cells required to generate a detectable MEG signal ranges from 10,000 to 50,000, with the majority of the signal arising from laminae II/III and V (*91*). Neuronal density varies substantially across the

cortex, from approximately 20,000 cells/mm^2 in frontal regions to around 45,000 in sensorimotor areas and up to 90,000 in the foveal region of primary visual cortex (V1; *98*). Factors such as cortical thickness, gyrification, and orientation of cortical columns relative to the sensors further constrain spatial resolution and depth precision. However, even with conventional MEG recording (without head-casts), spatial resolution as fine as ~1 mm^2 in V1 (*99*, *100*) and ~3.5 mm^2 in the sensorimotor cortex (*101*) has been demonstrated. Given the enhancements offered by hpMEG, achieving laminar resolution is a realistic goal. If it is possible to resolve a source on the cortical surface with millimeter precision, the same principles should, in theory, allow for distinguishing sources at different cortical depths provided the right conditions are met.

Our results demonstrate that constant source orientation across layers may not be appropriate for laminar inference, opening the possibility of using piecewise estimates of cortical column curvature. Cortical columns are not strictly straight (*102*), and future models could incorporate curvature by combining depth-varying orientation vectors derived from equivolumetric laminar surfaces (*75*, *103*), as opposed to the equidistant surfaces used here. Estimating cortical column orientation using diffusion tensor imaging (DTI) is a promising alternative, as anisotropic diffusion within cortical gray matter can reflect the organization of cortical columns (*104*, *105*). However, DTI-based estimates can be confounded by white matter fibers projecting into the cortex (the gyral bias effect), potentially biasing orientation measures. Advanced diffusion imaging techniques such as high angular resolution diffusion imaging (HARDI) and constrained spherical deconvolution, combined with surface-based analyses that sample diffusion metrics along radial cortical trajectories, can help isolate cortical diffusion signals from adjacent white matter influences (*106*, *107*). Integrating these advanced imaging approaches into laminar MEG source models could yield more biologically plausible dipole orientation estimates and potentially improve depth localization, especially in highly folded cortex. The current framework provides a foundation for evaluating such models and for testing how column curvature influences laminar MEG source reconstructions.

Given these constraints, it is natural to ask how hpMEG compares to ultra-high field fMRI (7 - 11.7 Tesla) for laminar investigations. While fMRI provides spatially precise laminar profiles, it is fundamentally limited by its reliance on the hemodynamic response, which is subject to vascular drainage effects (*108*). Efforts to mitigate this issue, such as deconvolution (*109*), vascular correction techniques (*110*), and contrast-based experimental designs (*111*), have improved laminar fMRI but do not fully resolve this limitation. Another important limitation of fMRI is its low temporal resolution (e.g. ~12 s per whole-brain acquisition at 0.8 mm resolution; , *112*). As a result, many studies restrict laminar fMRI acquisition to a limited part of the brain in order to achieve better temporal resolution. hpMEG, in contrast, provides direct neuronal measurements over the whole brain at millisecond resolution and is unaffected by vascular artifacts, making it uniquely suited for studying activity with rapid laminar dynamics such as beta bursts (*56*, *113*), induced oscillatory activity (*57*), and event-related responses. However, because MEG requires anatomical imaging to define laminar boundaries, its accuracy depends on high-quality MRI-derived cortical reconstructions. Although recent attempts have been made to generate individualized laminar maps over the whole cortex using multimodal MRI and machine learning (*114–118*), accurately achieving this for the whole cortex remains a major technical challenge. Successfully addressing this issue will require integrating advanced multimodal imaging

approaches, ultra-high-field MRI, movement correction, and sophisticated computational methods. Current hpMEG analyses must therefore rely on laminar histological atlases based on a single, *ex vivo* brain such as the BigBrain atlas (*74*, *75*). Developing methods for individualized laminar boundary estimation *in vivo* would represent a major step forward in both hpMEG and laminar fMRI research.

Given that lead field separation between superficial and deep cortical layers emerged as the strongest anatomical predictor of laminar inference accuracy, our results highlight the importance of accurate forward modeling. Our analyses, and all previous laminar MEG studies, relied on a simple single-shell forward model (*64*), which may underestimate differences in lead fields across cortical depths. Future work could improve laminar inference precision by employing more sophisticated forward models, such as boundary element models (BEM; *119*) or finite element models (FEM; *120*), which explicitly incorporate tissue-specific conductivity profiles. Recent methodological advancements improve FEM by integrating DTI-based conductivity tensors (*121*), offering another compelling route to combine MEG with DTI data to refine laminar specificity in source localization.

Emerging OPM technologies hold promise for further enhancing laminar inference by offering improved signal quality, allowing flexible sensor placement, and reducing operational costs (*79*, *80*, *122*). While still in its early stages, simulation studies suggest that OPM-based MEG, if configured correctly, can achieve laminar resolution comparable to classic, SQUID-based MEG, at least for bilaminar models (*123*). Future work should assess whether these benefits extend to full six-laminar inference. Both our results and those of Helbling (*123*) suggest that incorporating individual anatomical features such as cortical thickness and curvature could optimize OPM sensor placement to capture higher spatial-frequency components of the magnetic fields or achieve higher effective SNRs, potentially improving laminar precision within targeted cortical regions. Simulations could help refine these configurations, eliminating the need for time-consuming trial-and-error adjustments. Such targeted precision may be particularly useful for pre-surgical mapping of eloquent cortical regions or for resolving laminar-specific computations in particular regions of interest.

In summary, we establish hpMEG as a viable tool for non-invasive laminar inference, defining the conditions under which true depth-resolved localization is possible. By systematically exploring the trade-offs between signal quality, anatomical constraints, and inference accuracy, we delineate best-case and marginal conditions for MEG-based laminar inference. While current implementations require restrictive priors and high SNR, future developments, including Bayesian model averaging, individualized laminar and orientation priors, more accurate forward models, and emerging sensor technologies, may further improve hpMEG's ability to resolve cortical computations at the laminar level. These advances pave the way for a new era of laminar human neuroscience, bridging invasive electrophysiology with whole-brain, millisecond-resolution functional imaging.

References

1. C. U. M. Smith, A century of cortical architectonics. *J. Hist. Neurosci.* **1**, 201–218 (1992).

2. J. A. Hirsch, L. M. Martinez, Laminar processing in the visual cortical column. *Curr. Opin. Neurobiol.* **16**, 377–384 (2006).

3. H. Barbas, General Cortical and Special Prefrontal Connections: Principles from Structure to Function. *Annu. Rev. Neurosci.* **38**, 269–289 (2015).

4. R. J. Douglas, K. A. C. Martin, NEURONAL CIRCUITS OF THE NEOCORTEX. *Annu. Rev. Neurosci.* **27**, 419–451 (2004).

5. K. D. Harris, T. D. Mrsic-Flogel, Cortical connectivity and sensory coding. *Nature* **503**, 51–58 (2013).

6. K. D. Harris, G. M. G. Shepherd, The neocortical circuit: themes and variations. *Nat. Neurosci.* **18**, 170–181 (2015).

7. R. A. Adams, S. Shipp, K. J. Friston, Predictions not commands: active inference in the motor system. *Brain Struct. Funct.* **218**, 611–643 (2013).

8. L. H. Arnal, A.-L. Giraud, Cortical oscillations and sensory predictions. *Trends Cogn. Sci.* **16**, 390–398 (2012).

9. L. F. Barrett, W. K. Simmons, Interoceptive predictions in the brain. *Nat. Rev. Neurosci.* **16**, 419–429 (2015).

10. A. M. Bastos, R. Loonis, S. Kornblith, M. Lundqvist, E. K. Miller, Laminar recordings in frontal cortex suggest distinct layers for maintenance and control of working memory. *Proc. Natl. Acad. Sci.* **115**, 1117–1122 (2018).

11. A. M. Bastos, W. M. Usrey, R. A. Adams, G. R. Mangun, P. Fries, K. J. Friston, Canonical Microcircuits for Predictive Coding. *Neuron* **76**, 695–711 (2012).

12. M. Bennett, An Attempt at a Unified Theory of the Neocortical Microcircuit in Sensory Cortex. *Front. Neural Circuits* **14**, 40 (2020).

13. M. Bijanzadeh, L. Nurminen, S. Merlin, A. M. Clark, A. Angelucci, Distinct Laminar Processing of Local and Global Context in Primate Primary Visual Cortex. *Neuron* **100**, 259-274.e4 (2018).

14. H. Bowman, D. J. Collins, A. K. Nayak, D. Cruse, Is predictive coding falsifiable? *Neurosci. Biobehav. Rev.* **154**, 105404 (2023).

15. F. Capone, M. Paolucci, F. Assenza, N. Brunelli, L. Ricci, L. Florio, V. Di Lazzaro, Canonical cortical circuits: current evidence and theoretical implications. *Neurosci. Neuroeconomics* **5**, 1–8 (2016).

16. J. A. van Dijk, A. Fracasso, N. Petridou, S. O. Dumoulin, Laminar processing of numerosity supports a canonical cortical microcircuit in human parietal cortex. *Curr. Biol.* **31**, 4635-4640.e4 (2021).

17. S. Haar, O. Donchin, A Revised Computational Neuroanatomy for Motor Control. *J. Cogn. Neurosci.* **32**, 1823–1836 (2020).

18. S. Huang, S. J. Wu, G. Sansone, L. A. Ibrahim, G. Fishell, Layer 1 neocortex: gating and integrating multidimensional signals. *Neuron* **112**, 184–200 (2024).

19. W. A. Phillips, T. Bachmann, M. W. Spratling, L. Muckli, L. S. Petro, T. Zolnik, Cellular psychology: relating cognition to context-sensitive pyramidal cells. *Trends Cogn. Sci.* **29**, 28–40 (2025).

20. P. Wang, T. R. Knösche, A Realistic Neural Mass Model of the Cortex with Laminar-Specific Connections and Synaptic Plasticity – Evaluation with Auditory Habituation. *PLOS ONE* **8**, e77876 (2013).

21. S. Borbély, K. Halasy, Z. Somogyvári, L. Détári, I. Világi, Laminar analysis of initiation and spread of epileptiform discharges in three in vitro models. *Brain Res. Bull.* **69**, 161–167 (2006).

22. J. S. Ebersole, A. B. Chatt, Laminar interactions during neocortical epileptogenesis. *Brain Res.* **298**, 253–271 (1984).

23. C. F. Underwood, L. C. Parr-Brownlie, Primary motor cortex in Parkinson's disease: Functional changes and opportunities for neurostimulation. *Neurobiol. Dis.* **147**, 105159 (2021).

24. A. K. Engel, C. K. E. Moll, I. Fried, G. A. Ojemann, Invasive recordings from the human brain: clinical insights and beyond. *Nat. Rev. Neurosci.* **6**, 35–47 (2005).

25. R. Mukamel, I. Fried, Human Intracranial Recordings and Cognitive Neuroscience. *Annu. Rev. Psychol.* **63**, 511–537 (2012).

26. A. Pigorini, P. Avanzini, A. Barborica, C.-G. Bénar, O. David, M. Farisco, C. J. Keller, A. Manfridi, E. Mikulan, A. C. Paulk, N. Roehri, A. Subramanian, S. Vulliémoz, R. Zelmann, Simultaneous invasive and non-invasive recordings in humans: A novel Rosetta stone for deciphering brain activity. *J. Neurosci. Methods* **408**, 110160 (2024).

27. N. A. Steinmetz, C. Aydin, A. Lebedeva, M. Okun, M. Pachitariu, M. Bauza, M. Beau, J. Bhagat, C. Böhm, M. Broux, S. Chen, J. Colonell, R. J. Gardner, B. Karsh, F. Kloosterman, D. Kostadinov, C. Mora-Lopez, J. O'Callaghan, J. Park, J. Putzeys, B. Sauerbrei, R. J. J. Van Daal, A. Z. Vollan, S. Wang, M. Welkenhuysen, Z. Ye, J. T. Dudman, B. Dutta, A. W. Hantman, K. D. Harris, A. K. Lee, E. I. Moser, J. O'Keefe, A. Renart, K. Svoboda, M. Häusser, S. Haesler, M. Carandini, T. D. Harris, Neuropixels 2.0: A miniaturized high-density probe for stable, long-term brain recordings. *Science* **372**, eabf4588 (2021).

28. J. E. Chung, K. K. Sellers, M. K. Leonard, L. Gwilliams, D. Xu, M. E. Dougherty, V. Kharazia, S. L. Metzger, M. Welkenhuysen, B. Dutta, High-density single-unit human cortical recordings using the Neuropixels probe. *Neuron* **110**, 2409–2421 (2022).

29. S. L. Gratiy, A. Devor, G. T. Einevoll, A. M. Dale, On the estimation of population-specific synaptic currents from laminar multielectrode recordings. *Front. Neuroinformatics* **5**, 32 (2011).

30. L. Caruso, T. Wunderle, C. M. Lewis, J. Valadeiro, V. Trauchessec, J. T. Rosillo, J. P. Amaral, J. Ni, P. Jendritza, C. Fermon, S. Cardoso, P. P. Freitas, P. Fries, M. Pannetier-Lecoeur, In Vivo Magnetic Recording of Neuronal Activity. *Neuron* **95**, 1283-1291.e4 (2017).

31. B. R. Rosen, R. L. Savoy, fMRI at 20: Has it changed the world? *NeuroImage* **62**, 1316–1324 (2012).

32. D. L. Schomer, E. Niedermeyer, F. H. Lopes da Silva, Eds., *Niedermeyer's Electroencephalography: Basic Principles, Clinical Applications, and Related Fields* (Wolters Kluwer, Lippincott Williams & Wilkins, Philadelphia, Pa. London, 6. ed., 2011).

33. P. J. Uhlhaas, P. Liddle, D. E. J. Linden, A. C. Nobre, K. D. Singh, J. Gross, Magnetoencephalography as a Tool in Psychiatric Research: Current Status and Perspective. *Biol. Psychiatry Cogn. Neurosci. Neuroimaging* **2**, 235–244 (2017).

34. S. Baillet, Magnetoencephalography for brain electrophysiology and imaging. *Nat. Neurosci.* **20**, 327–339 (2017).

35. F. L. da Silva, EEG and MEG: Relevance to Neuroscience. *Neuron* **80**, 1112–1128 (2013).

36. M. Hämäläinen, R. Hari, R. J. Ilmoniemi, J. Knuutila, O. V. Lounasmaa, Magnetoencephalography---theory, instrumentation, and applications to noninvasive studies of the working human brain. *Rev. Mod. Phys.* **65**, 413–497 (1993).

37. R. Hari, R. Salmelin, Magnetoencephalography: From SQUIDs to neuroscience. *NeuroImage* **61**, 386–396 (2012).

38. A. Hillebrand, K. D. Singh, I. E. Holliday, P. L. Furlong, G. R. Barnes, A new approach to neuroimaging with magnetoencephalography. *Hum. Brain Mapp.* **25**, 199–211 (2005).

39. R. M. Leahy, J. C. Mosher, M. E. Spencer, M. X. Huang, J. D. Lewine, A study of dipole localization accuracy for MEG and EEG using a human skull phantom. *Electroencephalogr. Clin. Neurophysiol.* (1998).

40. J. Malmivuo, Comparison of the Properties of EEG and MEG in Detecting the Electric Activity of the Brain. *Brain Topogr.* **25**, 1–19 (2012).

41. R. B. Buxton, The physics of functional magnetic resonance imaging (fMRI). *Rep. Prog. Phys.* **76**, 096601 (2013).

42. N. K. Logothetis, What we can do and what we cannot do with fMRI. *Nature* **453**, 869–878 (2008).

43. R. A. Poldrack, The role of fMRI in Cognitive Neuroscience: where do we stand? *Curr. Opin. Neurobiol.* **18**, 223–227 (2008).

44. S. J. D. Lawrence, E. Formisano, L. Muckli, F. P. De Lange, Laminar fMRI: Applications for cognitive neuroscience. *NeuroImage* **197**, 785–791 (2019).

45. D. G. Norris, J. R. Polimeni, Laminar (f)MRI: A short history and future prospects. *NeuroImage* **197**, 643–649 (2019).

46. M. W. Self, T. van Kerkoerle, R. Goebel, P. R. Roelfsema, Benchmarking laminar fMRI: Neuronal spiking and synaptic activity during top-down and bottom-up processing in the different layers of cortex. *NeuroImage* **197**, 806–817 (2019).

47. J. Yang, L. Huber, Y. Yu, P. A. Bandettini, Linking cortical circuit models to human cognition with laminar fMRI. *Neurosci. Biobehav. Rev.* **128**, 467–478 (2021).

48. S. Haufe, R. Tomioka, T. Dickhaus, C. Sannelli, B. Blankertz, G. Nolte, K.-R. Müller, Large-scale EEG/MEG source localization with spatial flexibility. *NeuroImage* **54**, 851–859 (2011).

49. O. Hauk, M. Stenroos, M. S. Treder, Towards an objective evaluation of EEG/MEG source estimation methods – The linear approach. *NeuroImage* **255**, 119177 (2022).

50. J. Mattout, C. Phillips, W. D. Penny, M. D. Rugg, K. J. Friston, MEG source localization under multiple constraints: An extended Bayesian framework. *NeuroImage* **30**, 753–767 (2006).

51. J. G. Samuelsson, N. Peled, F. Mamashli, J. Ahveninen, M. S. Hämäläinen, Spatial fidelity of MEG/EEG source estimates: A general evaluation approach. *NeuroImage* **224**, 117430 (2021).

52. L. Troebinger, J. D. López, A. Lutti, S. Bestmann, G. Barnes, Discrimination of cortical laminae using MEG. *NeuroImage* **102**, 885–893 (2014).

53. J. Bonaiuto, H. E. Rossiter, S. S. Meyer, N. Adams, S. Little, M. F. Callaghan, F. Dick, S. Bestmann, G. R. Barnes, Non-invasive laminar inference with MEG: Comparison of methods and source inversion algorithms. *NeuroImage* **167**, 372–383 (2018).

54. L. Troebinger, J. D. López, A. Lutti, D. Bradbury, S. Bestmann, G. Barnes, High precision anatomy for MEG. *NeuroImage* **86**, 583–591 (2014).

55. S. S. Meyer, J. Bonaiuto, M. Lim, H. Rossiter, S. Waters, D. Bradbury, S. Bestmann, M. Brookes, M. F. M. F. M. F. Callaghan, N. Weiskopf, G. R. Barnes, Flexible head-casts for high spatial precision MEG. *J. Neurosci. Methods* **276**, 38–45 (2017).

56. M. J. Szul, S. Papadopoulos, S. Alavizadeh, S. Daligaut, D. Schwartz, J. Mattout, J. J. Bonaiuto, Diverse beta burst waveform motifs characterize movement-related cortical dynamics. *Prog. Neurobiol.* **228**, 102490 (2023).

57. J. Bonaiuto, S. S. Meyer, S. Little, H. Rossiter, M. F. Callaghan, F. Dick, G. R. Barnes, S. Bestmann, Lamina-specific cortical dynamics in human visual and sensorimotor cortices. *eLife* **7**, e33977 (2018).

58. J. J. Bonaiuto, S. Little, S. A. Neymotin, S. R. Jones, G. R. Barnes, S. Bestmann, Laminar dynamics of high amplitude beta bursts in human motor cortex. *NeuroImage* **242**, 118479 (2021).

59. B. Fischl, FreeSurfer. *NeuroImage* **62**, 774–781 (2012).

60. A. M. Dale, B. Fischl, M. I. Sereno, Cortical Surface-Based Analysis: I. Segmentation and Surface Reconstruction. *NeuroImage* **9**, 179–194 (1999).

61. J. Bonaiuto, F. Afdideh, M. Ferez, K. Wagstyl, J. Mattout, M. Bonnefond, G. R. Barnes, S. Bestmann, Estimates of cortical column orientation improve MEG source inversion. *NeuroImage* **216**, 116862 (2020).

62. W. Schroeder, K. M. Martin, W. E. Lorensen, *The Visualization Toolkit an Object-Oriented Approach to 3D Graphics* (Prentice-Hall, Inc., 1998;

https://dl.acm.org/doi/abs/10.5555/272980).

63. J. Ashburner, G. Barnes, C.-C. Chen, J. Daunizeau, G. Flandin, K. Friston, S. Kiebel, J. Kilner, V. Litvak, R. Moran, SPM12 manual. *Wellcome Trust Cent. Neuroimaging Lond. UK* **2464** (2014).

64. G. Nolte, The magnetic lead field theorem in the quasi-static approximation and its use for magnetoenchephalography forward calculation in realistic volume conductors. *Phys. Med. Biol.* **48**, 3637–3652 (2003).

65. A. M. Dale, M. I. Sereno, Improved Localizadon of Cortical Activity by Combining EEG and MEG with MRI Cortical Surface Reconstruction: A Linear Approach. *J. Cogn. Neurosci.* **5**, 162–176 (1993).

66. M. Fuchs, M. Wagner, H.-A. Wischmann, K. Ottenberg, O. Dössel, “Possibilities of Functional Brain Imaging Using a Combination of MEG and MRT” in *Oscillatory Event-Related Brain Dynamics* (Springer US, Boston, MA, 1994; http://link.springer.com/10.1007/978-1-4899-1307-4_31), pp. 435–457.

67. M. Hämäläinen, R. Hari, “Magnetoencephalographic (MEG) characterization of dynamic brain activation” in *Brain Mapping: The Methods*, A. Toga and J. Mazziotta, Ed. (Academic Press, Amsterdam, 2002), pp. 227–254.

68. A. Hillebrand, G. R. Barnes, The use of anatomical constraints with MEG beamformers. *NeuroImage* **20**, 2302–13 (2003).

69. F.-H. Lin, J. W. Belliveau, A. M. Dale, M. S. Hämäläinen, Distributed current estimates using cortical orientation constraints. *Hum. Brain Mapp.* **27**, 1–13 (2006).

70. K. Brodmann, *Vergleichende Lokalisationslehre Der Grosshirnrinde in Ihren Prinzipien Dargestellt Auf Grund Des Zellenbaues* (Barth, 1909).

71. C. F. von Economo, G. N. Koskinas, *Die Cytoarchitektonik Der Hirnrinde Des Erwachsenen Menschen* (J. Springer, 1925).

72. K. Wagstyl, L. Ronan, I. M. Goodyer, P. C. Fletcher, Cortical thickness gradients in structural hierarchies. *Neuroimage* **111**, 241–250 (2015).

73. K. Friston, L. Harrison, J. Daunizeau, S. Kiebel, C. Phillips, N. Trujillo-Barreto, R. Henson, G. Flandin, J. Mattout, Multiple sparse priors for the M/EEG inverse problem. *NeuroImage* **39**, 1104–1120 (2008).

74. K. Wagstyl, S. Larocque, G. Cucurull, C. Lepage, J. P. Cohen, S. Bludau, N. Palomero-Gallagher, L. B. Lewis, T. Funck, H. Spitzer, BigBrain 3D atlas of cortical layers: Cortical and laminar thickness gradients diverge in sensory and motor cortices. *PLoS Biol.* **18**, e3000678 (2020).

75. K. Wagstyl, C. Lepage, S. Bludau, K. Zilles, P. C. Fletcher, K. Amunts, A. C. Evans, Mapping Cortical Laminar Structure in the 3D BigBrain. *Cereb. Cortex* **28**, 2551–2562 (2018).

76. B. Fischl, M. I. Sereno, R. B. H. Tootell, A. M. Dale, High-resolution intersubject averaging and a coordinate system for the cortical surface. *Hum. Brain Mapp.* **8**, 272–284 (1999).

77. P. Belardinelli, E. Ortiz, G. R. Barnes, U. Noppeney, H. Preissl, Source reconstruction accuracy of MEG and EEG Bayesian inversion approaches. *PloS One* **7**, e51985 (2012).

78. J. D. López, V. Litvak, J. J. Espinosa, K. Friston, G. R. Barnes, Algorithmic procedures for Bayesian MEG/EEG source reconstruction in SPM. *NeuroImage* **84**, 476–487 (2014).

79. T. M. Tierney, N. Holmes, S. Mellor, J. D. López, G. Roberts, R. M. Hill, E. Boto, J. Leggett, V. Shah, M. J. Brookes, R. Bowtell, G. R. Barnes, Optically pumped magnetometers: From quantum origins to multi-channel magnetoencephalography. *NeuroImage* **199**, 598–608 (2019).

80. M. J. Brookes, J. Leggett, M. Rea, R. M. Hill, N. Holmes, E. Boto, R. Bowtell, Magnetoencephalography with optically pumped magnetometers (OPM-MEG): the next generation of functional neuroimaging. *Trends Neurosci.* **45**, 621–634 (2022).

81. T. P. Gutteling, M. Bonnefond, T. Clausner, S. Daligault, R. Romain, S. Mitryukovskiy, W. Fourcault, V. Josselin, M. Le Prado, A. Palacios-Laloy, A new generation of OPM for high dynamic and large bandwidth MEG: the 4He OPMs—first applications in healthy volunteers. *Sensors* **23**, 2801 (2023).

82. T. M. Fragoso, W. Bertoli, F. Louzada, Bayesian Model Averaging: A Systematic Review and Conceptual Classification. *Int. Stat. Rev.* **86**, 1–28 (2018).

83. M. Hinne, Q. F. Gronau, D. van den Bergh, E.-J. Wagenmakers, A Conceptual Introduction to Bayesian Model Averaging. *Adv. Methods Pract. Psychol. Sci.* **3**, 200–215 (2020).

84. G. Buzsáki, C. A. Anastassiou, C. Koch, The origin of extracellular fields and currents — EEG, ECoG, LFP and spikes. *Nat. Rev. Neurosci.* **13**, 407 (2012).

85. U. Mitzdorf, Current source-density method and application in cat cerebral cortex: investigation of evoked potentials and EEG phenomena. *Physiol. Rev.* **65**, 37–100 (1985).

86. K. H. Pettersen, A. Devor, I. Ulbert, A. M. Dale, G. T. Einevoll, Current-source density estimation based on inversion of electrostatic forward solution: Effects of finite extent of neuronal activity and conductivity discontinuities. *J. Neurosci. Methods* **154**, 116–133 (2006).

87. J. Potworowski, W. Jakuczun, S. Łęski, D. Wójcik, Kernel Current Source Density Method. *Neural Comput.* **24**, 541–575 (2012).

88. C. E. Tenke, J. Kayser, Generator localization by current source density (CSD): Implications of volume conduction and field closure at intracranial and scalp resolutions. *Clin. Neurophysiol.* **123**, 2328–2345 (2012).

89. D. Vidaurre, A. J. Quinn, A. P. Baker, D. Dupret, A. Tejero-Cantero, M. W. Woolrich, Spectrally resolved fast transient brain states in electrophysiological data. *NeuroImage* **126**, 81–95 (2016).

90. N. Klein, J. H. Siegle, T. Teichert, R. E. Kass, Cross-population coupling of neural activity based on Gaussian process current source densities. *PLOS Comput. Biol.* **17**, e1009601 (2021).

91. S. Murakami, Y. Okada, Contributions of principal neocortical neurons to magnetoencephalography and electroencephalography signals. *J. Physiol.* **575**, 925–936 (2006).

92. E. Boto, N. Holmes, J. Leggett, G. Roberts, V. Shah, S. S. Meyer, L. D. Muñoz, K. J. Mullinger, T. M. Tierney, S. Bestmann, G. R. Barnes, R. Bowtell, M. J. Brookes, Moving magnetoencephalography towards real-world applications with a wearable system. *Nature* **555**, 657–661 (2018).

93. W. Wang, F. Cao, N. An, W. Li, W. Xu, C. Wang, Z. Gao, D. Yu, Y. Gao, X. Ning, Design of locally arranged sensor arrays in wearable OPM-MEG based on sensor volume constraints. *Measurement* **229**, 114373 (2024).

94. A. Stolk, A. Todorovic, J.-M. Schoffelen, R. Oostenveld, Online and offline tools for head movement compensation in MEG. *NeuroImage* **68**, 39–48 (2013).

95. E. Messaritaki, L. Koelewijn, D. C. Dima, G. M. Williams, G. Perry, K. D. Singh, Assessment and elimination of the effects of head movement on MEG resting-state measures of oscillatory brain activity. *NeuroImage* **159**, 302–324 (2017).

96. S. Taulu, M. Kajola, Presentation of electromagnetic multichannel data: The signal space separation method. *J. Appl. Phys.* **97**, 124905 (2005).

97. S. Taulu, J. Simola, Spatiotemporal signal space separation method for rejecting nearby interference in MEG measurements. *Phys. Med. Biol.* **51**, 1759 (2006).

98. P. F. M. Ribeiro, L. Ventura-Antunes, M. Gabi, B. Mota, L. T. Grinberg, J. M. Farfel, R. E. P. Ferretti, R. Leite, W. Jacob Filho, S. Herculano-Houzel, The human cerebral cortex is neither one nor many: neuronal distribution reveals two quantitatively different zones in the gray matter, three in the white matter, and explains local variations in cortical folding. *Front. Neuroanat.* **7** (2013).

99. R. M. Cichy, F. M. Ramirez, D. Pantazis, Can visual information encoded in cortical columns be decoded from magnetoencephalography data in humans? *NeuroImage* **121**, 193–204 (2015).

100. K. Nasiotis, S. Clavagnier, S. Baillet, C. C. Pack, High-resolution retinotopic maps estimated with magnetoencephalography. *NeuroImage* **145**, 107–117 (2017).

101. E. L. Barratt, S. T. Francis, P. G. Morris, M. J. Brookes, Mapping the topological organisation of beta oscillations in motor cortex using MEG. *NeuroImage* **181**, 831–844 (2018).

102. S. Bok, Der Einfluss in den Furchen und Windungen auftretenden Krümmungen der Grosshirnrinde auf die Rindenarchitektur. *Z. Für Gesamte Neurol. Psychiatr.* **121**, 682–750 (1929).

103. M. D. Waehnert, J. Dinse, M. Weiss, M. N. Streicher, P. Waehnert, S. Geyer, R. Turner, P.-L. Bazin, Anatomically motivated modeling of cortical laminae. *NeuroImage* **93**, 210–220 (2014).

104. J. A. McNab, J. R. Polimeni, R. Wang, J. C. Augustinack, K. Fujimoto, A. Stevens, T. Janssens, R. Farivar, R. D. Folkerth, W. Vanduffel, L. L. Wald, Surface based analysis of diffusion orientation for identifying architectonic domains in the in vivo human cortex. *NeuroImage* **69**, 87–100 (2013).

105. C. W. U. Leuze, A. Anwander, P.-L. Bazin, B. Dhital, C. Stüber, K. Reimann, S. Geyer, R. Turner, Layer-Specific Intracortical Connectivity Revealed with Diffusion MRI. *Cereb. Cortex* **24**, 328–339 (2014).

106. O. F. Gulban, F. De Martino, A. T. Vu, E. Yacoub, K. Uğurbil, C. Lenglet, Cortical fibers orientation mapping using in-vivo whole brain 7 T diffusion MRI. *Neuroimage* **178**, 104–118 (2018).

107. E. St-Onge, A. Daducci, G. Girard, M. Descoteaux, Surface-enhanced tractography (SET). *NeuroImage* **169**, 524–539 (2018).

108. M. Havlicek, K. Uludağ, A dynamical model of the laminar BOLD response. *NeuroImage* **204**, 116209 (2020).

109. I. Markuerkiaga, J. P. Marques, T. E. Gallagher, D. G. Norris, Estimation of laminar BOLD activation profiles using deconvolution with a physiological point spread function. *J. Neurosci. Methods* **353**, 109095 (2021).

110. Y. Chai, L. Li, L. Huber, B. A. Poser, P. A. Bandettini, Integrated VASO and perfusion contrast: A new tool for laminar functional MRI. *NeuroImage* **207**, 116358 (2020).

111. J. R. Polimeni, B. Fischl, D. N. Greve, L. L. Wald, Laminar analysis of 7 T BOLD using an imposed spatial activation pattern in human V1. *NeuroImage* **52**, 1334–1346 (2010).

112. Y. Chai, A. T. Morgan, H. Xie, L. Li, L. Huber, P. A. Bandettini, B. P. Sutton, Unlocking near-whole-brain, layer-specific functional connectivity with 3D VAPER fMRI. *Imaging Neurosci.* **2**, 1–20 (2024).

113. H. Rayson, M. J. Szul, P. El-Khoueiry, R. Debnath, M. Gautier-Martins, P. F. Ferrari, N. Fox, J. J. Bonaiuto, Bursting with Potential: How Sensorimotor Beta Bursts Develop from Infancy to Adulthood. *J. Neurosci.* **43**, 8487–8503 (2023).

114. G. Chen, F. Wang, J. C. Gore, A. W. Roe, Identification of cortical lamination in awake monkeys by high resolution magnetic resonance imaging. *NeuroImage* **59**, 3441–3449 (2012).

115. R. Trampel, P.-L. Bazin, K. Pine, N. Weiskopf, In-vivo magnetic resonance imaging (MRI) of laminae in the human cortex. *NeuroImage* **197**, 707–715 (2019).

116. S. Kundu, S. Barsoum, J. Ariza, A. L. Nolan, C. S. Latimer, C. D. Keene, P. J. Basser, D. Benjamini, Mapping the individual human cortex using multidimensional MRI and unsupervised learning. *Brain Commun.* **5**, fcad258 (2023).

117. J. A. Autio, A. Uematsu, T. Ikeda, T. Ose, Y. Hou, L. Magrou, I. Kimura, M. Ohno, K. Murata, T. Coalson, H. Kennedy, M. F. Glasser, D. C. Van Essen, T. Hayashi, Charting cortical-layer specific area boundaries using Gibbs' ringing attenuated T1w/T2w-FLAIR myelin MRI. *bioRxiv*, 2024.09.27.615294 (2024).

118. X. Zeng, O. Puonti, A. Sayeed, R. Herisse, J. Mora, K. Evancic, D. Varadarajan, Y. Balbastre, I. Costantini, M. Scardigli, J. Ramazzotti, D. DiMeo, G. Mazzamuto, L. Pesce, N. Brady, F. Cheli, F. Saverio Pavone, P. R. Hof, R. Frost, J. Augustinack, A. Van Der Kouwe, J. Eugenio Iglesias, B. Fischl, Segmentation of supragranular and infragranular layers in ultra-high-resolution 7T *ex vivo* MRI of the human cerebral cortex. *Cereb. Cortex* **34**, bhae362 (2024).

119. M. Stenroos, A. Hunold, J. Haueisen, Comparison of three-shell and simplified volume conductor models in magnetoencephalography. *NeuroImage* **94**, 337–348 (2014).

120. T. Erdbrügger, M. Höltershinken, J.-O. Radecke, Y. Buschermöhle, F. Wallois, S. Pursiainen, J. Gross, R. Lencer, C. Engwer, C. Wolters, CutFEM-based MEG forward modeling improves source separability and sensitivity to quasi-radial sources: A somatosensory group study. *Hum. Brain Mapp.* **45**, e26810 (2024).

121. T. Medani, J. Garcia-Prieto, F. Tadel, M. Antonakakis, T. Erdbrügger, M. Höltershinken, W. Mead, S. Schrader, A. Joshi, C. Engwer, C. H. Wolters, J. C. Mosher, R. M. Leahy, Brainstorm-DUNEuro: An integrated and user-friendly Finite Element Method for modeling electromagnetic brain activity. *NeuroImage* **267**, 119851 (2023).

122. E. Labyt, M.-C. Corsi, W. Fourcault, A. Palacios Laloy, F. Bertrand, F. Lenouvel, G. Cauffet, M. Le Prado, F. Berger, S. Morales, Magnetoencephalography With Optically Pumped 4He Magnetometers at Ambient Temperature. *IEEE Trans. Med. Imaging* **38**, 90–98 (2019).

123. S. Helbling, Inferring laminar origins of MEG signals with optically pumped magnetometers (OPMs): A simulation study. *Imaging Neurosci.* **3**, imag_a_00410 (2025).

Acknowledgements
We gratefully acknowledge support from the CNRS/IN2P3 Computing Center (Lyon - France) for providing computing and data-processing resources needed for this work.

***Funding*:** This work was supported by the European Research Council (ERC) under the European Union's Horizon 2020 research and innovation programme (ERC consolidator grant 864550).

***Author contributions*:** Conceptualization, methodology, software, validation, formal analysis, investigation, visualization, writing—original draft, writing—review and editing, supervision, project administration, funding acquisition: J.J.B. Methodology, software, validation, formal analysis, visualization, writing—original draft: M.J.S. Conceptualization, writing—review and editing: S.B, and G.R.B. Writing—review and editing: B.H. Software, validation, visualization, writing—original draft: I.A. and Q.M.

***Competing interests*:** The authors declare that they have no competing interests.

***Data and materials availability*:** All data and code used in this study are available at https://github.com/danclab/multilaminar_sim/. Additional materials are provided in the Supplementary Figures.

Supplementary Figures

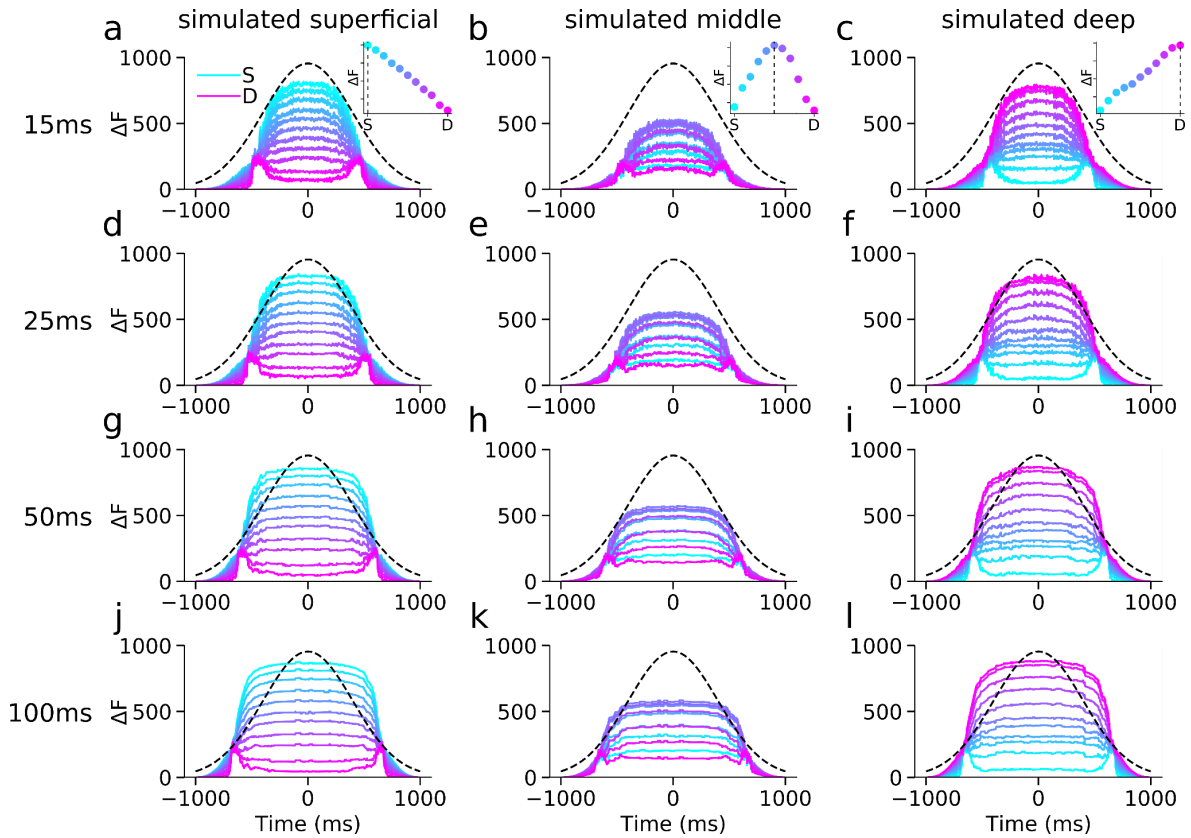

Figure S1. Effect of sliding window size on laminar inference accuracy. Laminar model evidence over time (ΔF, relative to worst model at each time point) for simulated dipolar sources across 11 cortical depths, shown for sliding window sizes of 15 ms, 25 ms, 50 ms, and 100 ms (rows). Columns correspond to sources simulated at superficial, middle, and deep cortical depths. Each trace reflects the average ΔF across 100 simulated cortical locations at a fixed sensor-level SNR of -20 dB. Colors indicate cortical evaluation depth (S = superficial surface layer, D = deep surface layer). The black dashed line shows the simulated signal time course. Inset panels in the first row (a-c) show model evidence at t = 0ms, with peak ΔF values aligning with the simulated source depth (dashed vertical line). The depth-specific pattern of model evidence was consistent across window sizes for each simulated depth (columns). Results confirm that laminar model discrimination is consistent across a wide range of window sizes, with all tested windows successfully recovering the correct source depth.

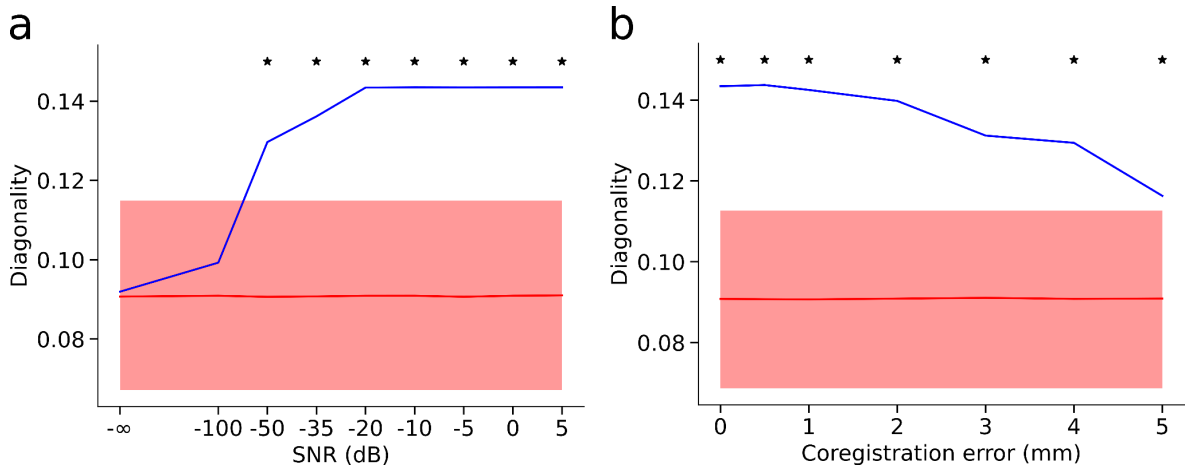

Figure S2. Diagonal-dominance scores for laminar model-evidence matrices across different SNR and coregistration error values. (a) Varying sensor-level SNR, and (b) varying co-registration error. Blue curves show observed diagonal dominance (trace / sum of each matrix), and red curves show the mean from permuted matrices with shaded 95% CI. Black stars mark SNR or co-registration levels where observed diagonal dominance differed significantly from chance ($p < 0.05$).

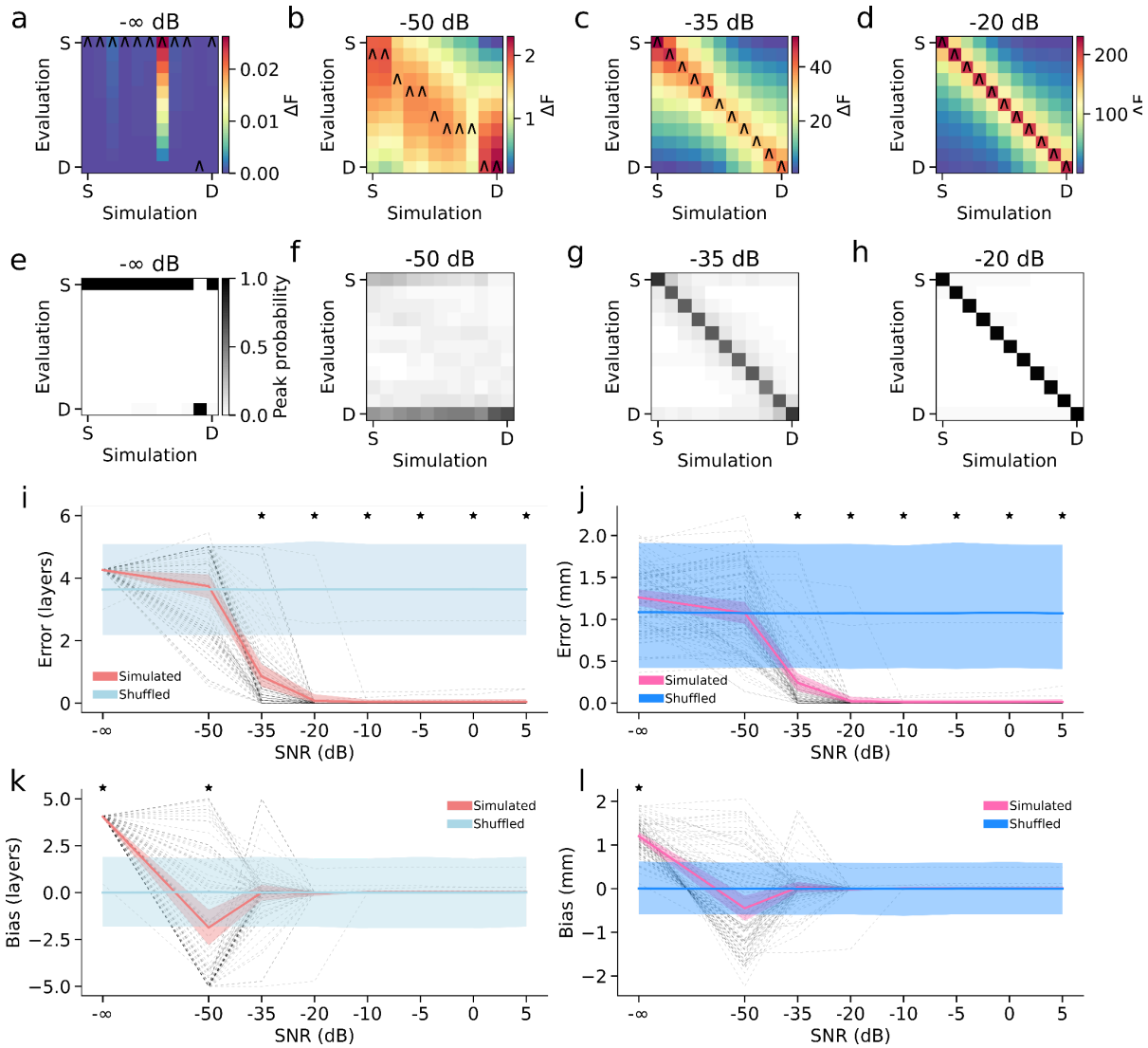

Figure S3. Laminar source-reconstruction accuracy with EBB as a function of SNR. a–d) Mean

model evidence (free energy, ΔF) matrices (row-normalized to the worst model; S = superficial surface layer, D = deep surface layer) for simulated signals placed on 11 cortical surfaces at four SNR levels (−∞ dB, −50 dB, −35 dB, −20 dB). Triangular markers denote the forward model with peak free energy for each simulated depth. **e–h)** Probability density of each forward model being the maximum-evidence solution, aggregated across cortical locations. **i, j)** Laminar reconstruction error (in layers and mm). **k, l)** Laminar reconstruction bias (in surface layers and millimeters), again comparing simulated and shuffled data. Shaded bands represent 95% confidence intervals, and asterisks mark SNR levels at which observed error or bias differed significantly from chance ($p < 0.05$).

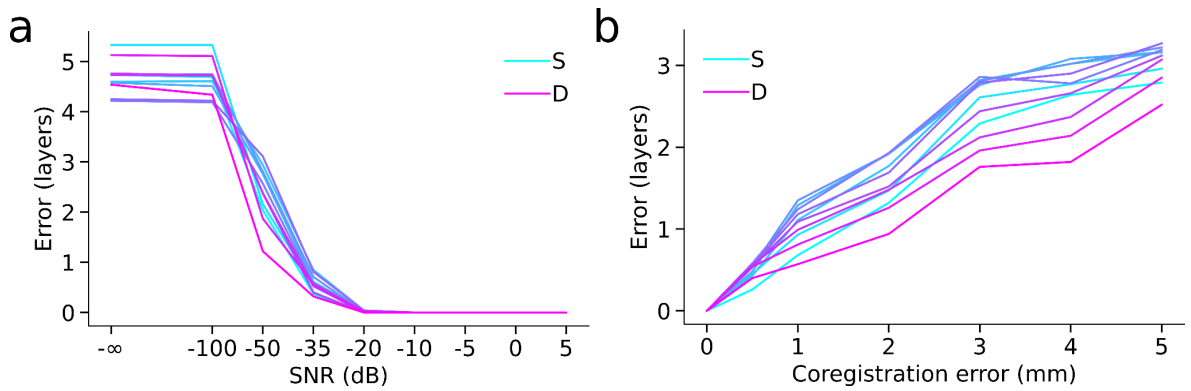

Figure S4. Layer-by-layer source-reconstruction error. (a) Mean error as a function of SNR for each simulation surface layer, from superficial (S, light cyan) to deep (D, magenta). (b) Corresponding layer-by-layer error over increasing co-registration error.

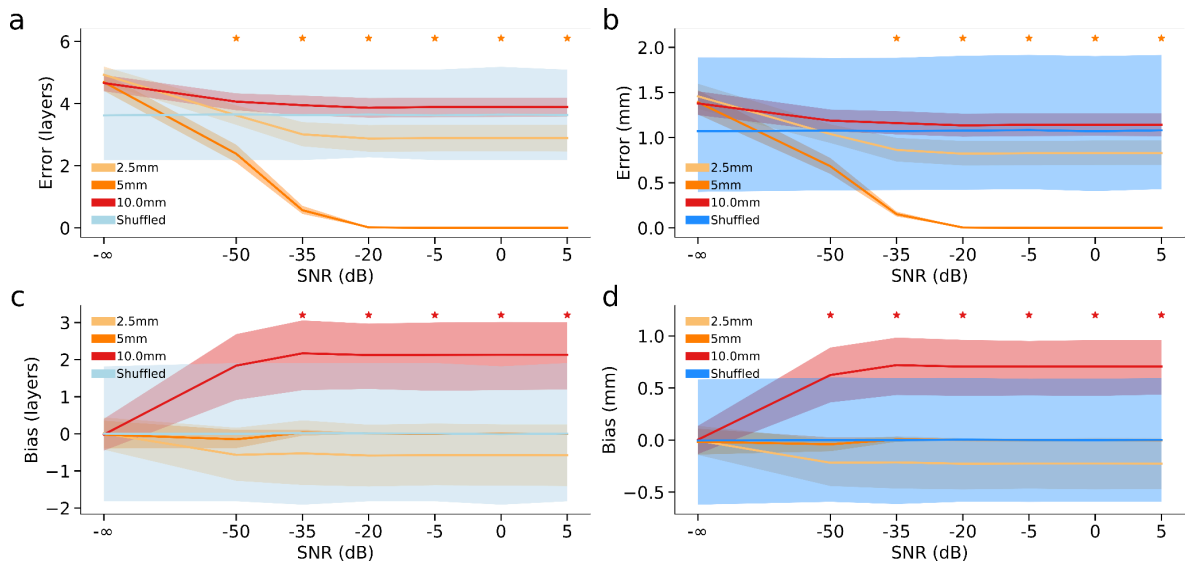

Figure S5. Effect of patch size mismatch on laminar source reconstruction accuracy across SNR levels. a,b) Laminar source reconstruction error (in layers and mm) falls below chance at higher SNR only when the patch size of the source reconstruction model matches that of the simulated data (5mm in these simulations). **c,d)** Over-estimation of patch size biases laminar inference toward superficial layers, whereas under-estimation slightly biases toward deep layers. Shaded bands represent 95% confidence intervals, and asterisks mark SNR levels at which observed error or bias differed significantly from chance ($p < 0.05$).